

Statistical analysis of 26 yr of observations of decametric radio emissions from Jupiter[★]

M. S. Marques^{1,2}, P. Zarka^{2,3}, E. Echer¹, V. B. Ryabov⁴, M. V. Alves¹, L. Denis³, and A. Coffre³

¹ INPE, Sao Jose do Campos, Brazil
e-mail: manilo.marques@gmail.com

² LESIA, Observatoire de Paris, CNRS, PSL, UPMC/SU, UPD, Place J. Janssen, Meudon, France
e-mail: philippe.zarka@obspm.fr

³ Station de Radioastronomie de Nançay, Obs. Paris, CNRS, PSL, Univ. Orléans, Nançay, France

⁴ Complex and Intelligent Systems Department, Future Univ. Hakodate, Japan

Received 7 November 2016 / Accepted 10 April 2017

ABSTRACT

Jupiter is a complex and at the same time very powerful radio source in the decameter wavelength range. The emission is anisotropic, intrinsically variable at millisecond to hour timescales, and also modulated by various external processes at much longer periods, ranging from ~10 h to months or years (including Jovian day and year, solar activity and solar wind variations, and for ground-based observations, terrestrial day and year). As a consequence, long-term observations and their statistical study have proved to be necessary for disentangling and understanding the observed phenomena. We have built a database from the available 26 yr of systematic, daily observations conducted at the Nançay Decameter Array and recorded in digital format. This database contains all observed Jovian decametric emissions, classified with respect to the time-frequency morphology, their dominant circular polarization, and maximum frequency. We present the results of the first statistical analysis of this database. We confirm the earlier classification of Jovian decameter emissions in Io-A, -A', -B, -C, -D and non-Io-A, -B, -C types, but we also introduce new emission types (Io-A'' and Io-B') and precise and characterize the non-Io-D type. We determine the contours of all emission types in the CML- Φ_{10} plane (Central Meridian Longitude in Jupiter's System III coordinates versus Io Phase), provide representative examples of their typical time-frequency patterns, and the distribution of emission's maximum frequency as a function of Λ_{10} (Io's Longitude). Finally, we present a statistical analysis of the distributions of the occurrence rate, duration, intensity and polarization for each emission type. non-Io-DAM appears to be related to small-scale, possibly bursty auroral structures.

Key words. radiation mechanisms: non-thermal – methods: statistical – catalogs – planets and satellites: aurorae – planets and satellites: individuals: Jupiter

1. Introduction

The decameter radio emission (DAM) of Jupiter has been studied using ground-based observations since its discovery in 1955 (Burke & Franklin 1955). It was soon interpreted as cyclotron emission and thus provided constraints on the magnetic field amplitude of Jupiter, while its temporal modulation with period of about 10h provided a measure of the rotation of Jupiter (Carr et al. 1983; Genova et al. 1989). Since then, our knowledge has increased considerably. Today we know that DAM sources are distributed along Jovian magnetic field lines, along which keV electron precipitation occurs. These precipitations are either caused by the Io-Jupiter electrodynamic interaction or are related to auroral activity. At each altitude, emission is produced at or near the local electron cyclotron frequency f_{ce} , where $f_{ce} = \frac{eB}{2\pi m} \approx 2.8B$ (with f_{ce} in MHz and B is the magnetic field strength in Gauss). In the decameter range, the sources extend from the top of the atmosphere to an altitude of a few tenths of a Jovian radius. The generation mechanism has been convincingly identified as the cyclotron-maser instability (CMI), which

is similar to the generation mechanism of auroral kilometric radiation of the Earth (Wu & Lee 1979; Zarka 1998).

Decameter emissions are very complex and variable, consisting of several components modulated at all timescales from millisecond to weeks or months (e.g., Lecacheux et al. 2004):

- milliseconds to seconds: S-bursts (from Gallet 1961 to Ryabov et al. 2014);
- seconds to minutes: interplanetary and ionospheric scintillations (Genova et al. 1981) and modulation lanes (Imai et al. 1992);
- minutes to hours: arcs in the $t - f$ (time – frequency) plane (Boischot & Aubier 1981; Hess et al. 2008b,a);
- about ten hours: planetary rotation (Higgins et al. 1997);
- days to months: interplanetary shocks and response to solar wind (Terasawa et al. 1978; Zarka & Genova 1983; Hess et al. 2012, 2014).

At timescales from minutes to hours, most of the observed variations are related to geometrical visibility effects. The DAM emission beam is strongly anisotropic, being produced by the CMI mechanism at each point of the source along the walls of a hollow cone centered on the magnetic field line at the source. The half-aperture angle of this cone is large over most of the DAM range (often $\geq 60^\circ$; Queinnec & Zarka 1998; Zarka 1998)

[★] The database is only available in electronic form at the CDS via anonymous ftp to cdsarc.u-strasbg.fr (130.79.128.5) or via <http://cdsarc.u-strasbg.fr/viz-bin/qcat?J/A+A/604/A17>

and it varies with the observed frequency. Ray & Hess (2008) found that the beaming angle peaks in the range $\sim 10\text{--}15$ MHz and decreases toward lower and higher frequencies, whereas Imai et al. (2008) found that, for a different type of DAM, the beaming angle increases monotonically from 9 to 16 MHz.

The complex source structure (i.e., distributed sources in a complex Jovian magnetic field that have a strong contribution of multipolar terms in the range of altitudes corresponding to DAM) and anisotropic beaming, combined with various modulations by the planetary rotation, orbital motion of Io (and possibly other satellites), variable latitude of the observer during the Jovian year, and various external physical drivers (such as the solar wind), cause the observed complexity of the emission occurrence and $t - f$ morphology.

As a consequence, statistical studies based on long-term observations are required for distinguishing the several phenomena superimposed at various timescales and determining the emission properties. This is why systematic observations (synoptic monitoring programs) have been carried out at various radio observatories since the discovery of Jovian DAM (e.g., in Boulder, Florida, and Nançay). Based on these observations, extensive catalogs of the detected emissions at minute to hour timescales have been built (Thieman 1979; Leblanc et al. 1981, 1983, 1989, 1990, 1993).

The most notable early outcome of these statistical studies was the discovery of the Jovian DAM part controlled by the satellite Io (Bigg 1964). When plotting the occurrence probability as a function of orbital phase of Io (Φ_{Io} ; cf. Fig. 1), the DAM occurrence exhibits two strong peaks at $\Phi_{\text{Io}} \sim 90^\circ$ and $\sim 240^\circ$, revealing the existence of an Io-Jupiter electrodynamic interaction that causes electron acceleration and consequently decameter radio emission. Owing to the delay between the initial interaction between Io and the Jovian magnetic field and subsequent electron acceleration, the radio emitting – so-called active – field line is shifted from the instantaneous Io field line by up to $\sim 15^\circ$ (δ_a in Fig. 1; see also Fig. 6 in Zarka 2004). This shift is in the leading direction, i.e., ahead of Io along its orbital motion, because the magnetic field of Jupiter rotates faster than the orbital motion of Io, and hence sweeps Io from back to front relative to its motion (Saur et al. 2004). Taking this lead angle into account, one can conclude that the radio emitting field line is located at symmetrical positions relative to the Earth-Jupiter line when emission is detected (Fig. 2 in Zarka et al. 1996).

Based on this result, Bigg (1964) and others (Carr et al. 1983; Genova et al. 1989) split DAM emission events in two groups, one of which is related to Io (Io-DAM) and the other not related to it (non-Io-DAM). When emission occurrence is plotted as a function of CML (central meridian longitude, i.e., the Jovicentric longitude of the observer in Jovian System III (Higgins et al. 1996)) and Φ_{Io} , Io-DAM appears clearly in regions of enhanced occurrence probability limited in both CML and Φ_{Io} , whereas non-Io-DAM appears in intervals of CML independent of Φ_{Io} . The four main Io-DAM regions have been labeled A, B, C, and D (e.g., Carr et al. 1983; Genova et al. 1989). These regions have been later interpreted as sources located in the two hemispheres and at the two limbs of Jupiter. Further studies have shown that these four regions of enhanced occurrence actually correspond to two physical sources, one in each hemisphere. Because the radio beaming is at a large angle from the magnetic field in the source, each of these two sources can be observed from two different viewing geometries, near each limb of the planet (Queinnec & Zarka 1998; Zarka et al. 2011). This geometry of DAM emissions is illustrated in Fig. 2. The A and B emissions thus originate from the northern hemisphere

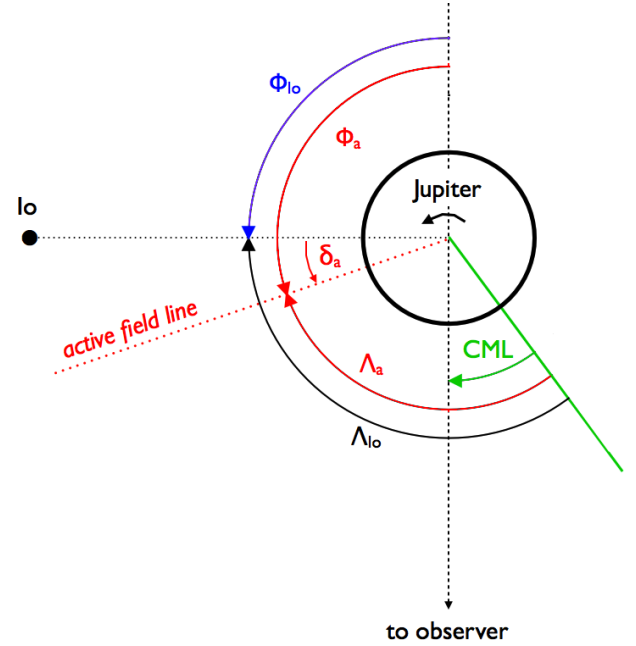


Fig. 1. Definition of the observer’s CML, Io phase Φ_{Io} and longitude Λ_{Io} . Lead angle δ_a , phase, and longitude of the radio-emitting active field line are shown in red.

footprints of the radio-emitting field line from the dusk and dawn sides of Jupiter as seen from Earth, respectively. The C and D emissions originate from the radio-emitting field line footprints in the southern hemisphere from the dusk and dawn sides of Jupiter, respectively. Io-induced emissions (Io-DAM) result from electrons accelerated by Io but emitting in the magnetic field of Jupiter. For simplicity, we hereafter call these Io emissions. Conversely, Io-independent emissions, likely to be of auroral origin, are simply called non-Io emissions.

Both Io and non-Io emissions appear in the $t - f$ plane as arcs. The arc shape was interpreted as resulting from the combination of the topology of the Jovian magnetic field, radio beaming, and observation geometry (Leblanc 1981; Carr et al. 1983; Zarka 1998; Hess et al. 2008a, 2014). The shape varies from one emission region to another. The B and D arcs have a so-called vertex-early shape (i.e., similar to an open parenthesis), whereas A and C arcs have a vertex-late shape (closed parenthesis). Schematics of arcs curvature are also shown in Fig. 2.

Moreover, the observed polarization of DAM is circular or elliptical, as it is mainly in the right-hand sense (RH) for emissions coming from the northern hemisphere (A and B regions), and in the left-hand sense (LH) for emissions coming from the southern hemisphere (C and D regions). The difference in the observed sense of polarization is related to the direction of the \mathbf{k} vector of the wave relative to that of the magnetic field vector \mathbf{B} in the source. In a northern magnetic hemisphere, \mathbf{B} points outward so that the angle (\mathbf{k}, \mathbf{B}) is acute and the polarization of the emitted radio wave (relative to \mathbf{k}) is thus the same as the polarization of the magneto-ionic X mode generated by the CMI, i.e., RH. In a southern magnetic hemisphere, \mathbf{B} points inward so that the angle (\mathbf{k}, \mathbf{B}) is obtuse and the RH wave (relative to \mathbf{B}) generated by the CMI is LH relative to \mathbf{k} . The observed polarization is thus LH in that case.

As the emission is generated at the local f_{ce} , its instantaneous maximum frequency corresponds to the magnetic field amplitude at or near the footprint of the emitting field line. This maximum frequency is generally higher for Io emission and in the

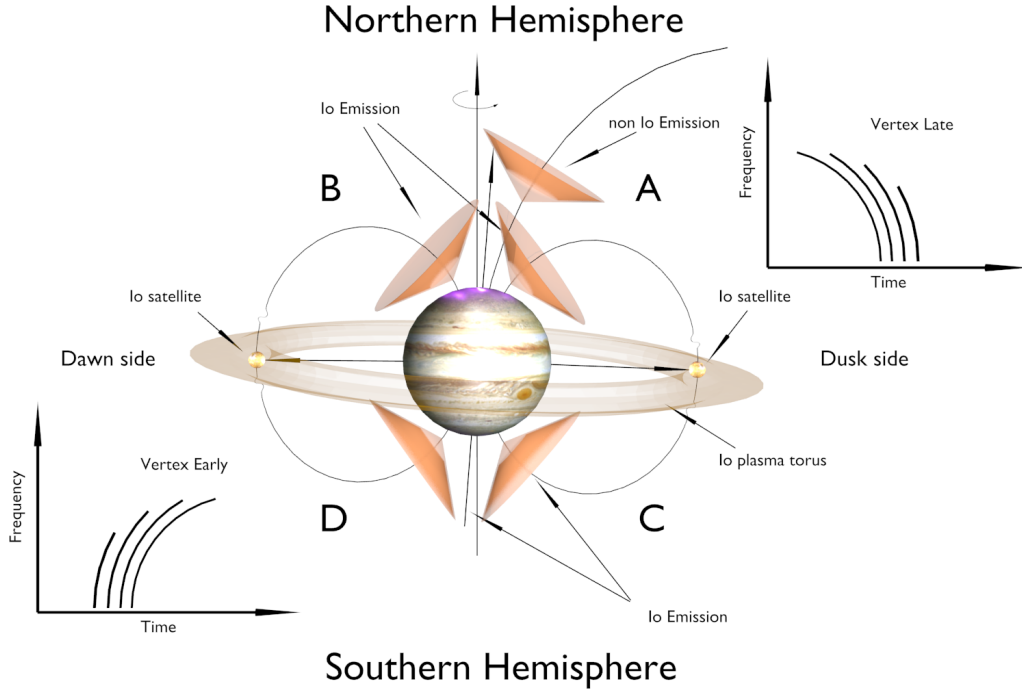


Fig. 2. Geometry and nomenclature of Io and non-Io emissions, and corresponding arc shapes in the $t - f$ plane. Emission is produced along the displayed conical sheets, and thus observable only when the source is near a limb of Jupiter. Dawn side sources produce vertex-early arcs whereas dusk side sources produce vertex-late arcs, as explained in Hess et al. (2014). The magnetic field line connected to Io is sketched as the active, radio-emitting field line but actually the active field line leads the instantaneous Io field line by several degrees (cf. Fig. 1).

northern hemisphere. Northern emissions are also more frequent than southern emissions.

As a consequence, the emission patterns corresponding to each of the regions (Io or non-Io, A, B, C, and D) have properties such as (i) the shape of radio arcs in the $t - f$ plane (typically vertex-early or vertex-late arcs); (ii) the detected wave polarization; and (iii) the maximum frequency reached during every DAM event, which can be used to identify the emission type. As this identification does not rely upon the location in the $CML - \Phi_{Io}$ plane corresponding to emission occurrence, it allows us to separate emissions of different types occurring in overlapping regions in the $CML - \Phi_{Io}$ plane. As shown below, this increases the statistical significance of the results. In this paper we applied this approach to classify DAM emissions recorded by the Nançay Decametric Array (NDA) in France, and we built a database (or catalog) over 26 yr of Jupiter observation, which is the longest time interval of this kind ever studied at once.

Section 2 describes the NDA and its observations. Section 3 describes the construction of the catalog and the methodology used to identify DAM events, and it presents some statistical properties of observations. Section 4 presents the statistical properties of Io and non-Io emissions determined through the analysis of our 26-yr catalog. This is followed by a summary and perspectives for the further exploitation of the catalog. Two appendices provide (A) further details on the construction of the catalog and (B) statistical properties of individual emission types.

2. Instrumentation and observations

The Nançay Decameter Array, built from 1975 to 1977, is a medium size phased array consisting of 144 log-spiral (so-called Tee-Pee) antennas, sensitive to the range $\sim 10 - 100$ MHz (Boischoit et al. 1980; Lecacheux et al. 2004). The antennas are

circularly polarized, 72 in the right-hand circular (RHC) sense and 72 in the left-hand circular (LHC) one. Each 72-antenna array is phased in two steps: by groups of 8 antennas and through delay lines. Each antenna has an effective area $\sim \lambda^2/3$, thus each polarized array of 72 antennas has an effective area $\sim 24\lambda^2$, limited to ~ 3500 m² owing to the overlap of antenna effective areas at low frequencies; the gain of each array is about 25 dB at 25 MHz. The system noise, or system equivalent flux density (SEFD), of the NDA is dominated by the Galactic background noise ($T \sim 60\lambda^{2.55}$), and this is $\sim 10^4$ Jy at 40 MHz.

As the sensitivity of the instrument is limited, it has been largely dedicated to the systematic observation of the strong and variable decameter radio sources, which are Jupiter and the Sun. Observations are carried out 8 h/day for each target from $-4h$ to $+4h$ of their meridian transit times, when these times are separated enough. When Jupiter and the Sun are less than 8h apart in right ascension, priority is given to one target or the other according to special requests, for example, in case of high solar activity, high probability of Io emission, and a support observation campaign for a space mission.

These systematic NDA observations (also called routine observations) have been performed since September 1990 using a swept-frequency analyzer that sweeps across the band 10–40 MHz, measuring alternatively one spectrum of LHC polarized intensity and one spectrum of RHC polarized intensity. This analyzer is connected to a PC that ensures digitization and data acquisition. One sweep takes 500 ms per spectrum, i.e., two consecutive spectra of same polarization are separated by 1 s. One spectrum consists of measurements at 400 frequencies separated by 75 kHz. The sweeping filter (channel) width is $b = 30$ kHz, leaving gaps of 45 kHz between measurements at two consecutive frequencies. As frequencies are explored consecutively, $\tau \sim 1.2$ ms is spent dwelling on every channel. The sensitivity

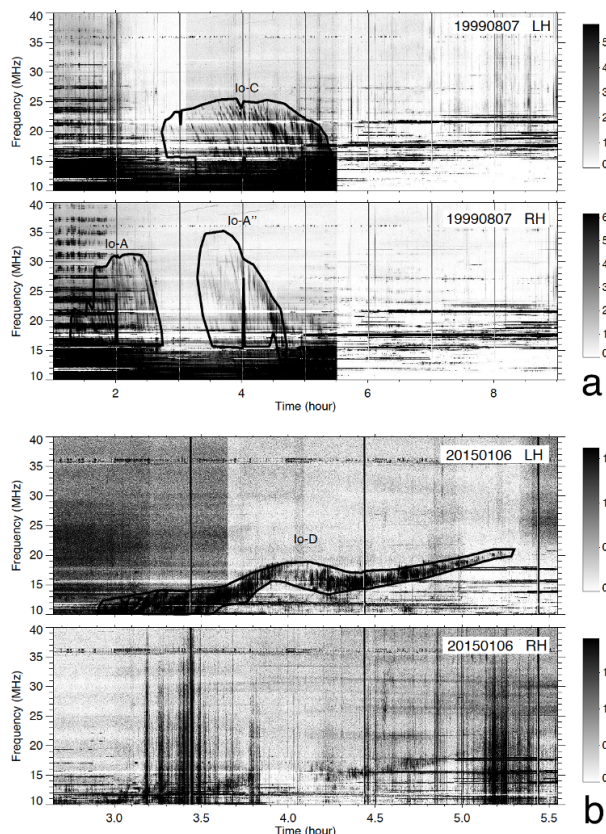


Fig. 3. Example of NDA routine dynamic spectra ($t - f$ displays) and emission contours drawn when building the catalog. The timescale is in UT of the day of Jupiter’s passage at the local meridian (i.e., if transit occurs at 01:00, data is recorded from -3 h to $+5$ h, whereas if transit occurs at 22:30, data is recorded from 18:30 to 26:30). **a)** Dynamic spectrum in LH and RH polarization of an observation recorded on 07/08/1999. Three types of Jovian emissions are detected: an LH (Io-C) and two RH emissions (Io-A and Io-A’) with weak or no counterparts in the opposite polarization. Hourly calibrations, various interference, and high-pass filter switch-on at 05:30 are clearly visible. **b)** Dynamic spectrum in LH and RH polarization of an observation recorded on 06/01/2015. The Io-D has LH elliptical polarization (as deduced from the “ghost” in RH polarization) and a peculiar $t - f$ shape.

of these routine observations is thus low; i.e., $\text{SEFD}/(b \times \tau)^{1/2} \approx 1500$ Jy.

Daily routine data can be represented conveniently as two dynamic spectra, LHC and RHC, with $1 \text{ s} \times 75 \text{ kHz}$ resolutions, covering the frequency range 10–40 MHz and lasting up to 8 h. Two typical observations are shown in Fig. 3. Every hour, a calibration sequence interrupts the sky signal for 40 s. It consists of broadband noise injected from a noise generator at the foot of each eight-antenna group, at four different intensity levels (for 10 s each). The lowest step is below the sky background level, and the others are 10, 20, and 30 dB stronger. The calibration sequence starts with the step with strongest noise intensity. Fixed-frequency interference (e.g., broadcast stations and radar signals) are visible as horizontal lines, especially in the low-frequency half of the dynamic spectra. These interferences are stronger during the day, thus a high-pass filter that attenuates signals below 20 MHz is automatically switched on from dawn to dusk. Sporadic broadband interference (e.g., lightning and electronics) are also observed, as well as variable background level that is partly due to the variable condition of the instrument between maintenance operations.

3. Nançay Decametric Array Jupiter catalog

As explained above, the determination of many DAM properties, constraining its generation scenario and its relation to the Jovian magnetospheric dynamics, requires statistical studies based on long-term observations. Several catalogs of Jovian DAM have been constructed from the NDA data since the start of its operations (Leblanc et al. 1981, 1983, 1989, 1990, 1993). These catalogs were built from the visual examination of recorded dynamic spectra in printed form (on paper or 35 mm film). The information listed in these catalogs is generally restricted to the start and end times of an emission and the overall spectral range that it covers (i.e., a single minimum and a single maximum frequency), defining a rectangular contour in the $t - f$ plane.

In order to build a more informative digital database of Jupiter emissions over the 26 yr of routine data available (from 1990 to 2015), a specific tool was designed. This tool allows us to display the dynamic spectra (simultaneously in LHC and RHC polarizations; cf. Fig. 3) and to catalog the emissions patterns (or events) that they contain. Emission recognition is visual because no automated procedure exists yet to recognize efficiently Jupiter emissions and distinguish them from interference.

The selection of the emission type relies on the shape of the event in the $t - f$ plane (vertex early and late arcs), its dominant polarization, and maximum frequency reached in the spectrogram. The first two criteria were briefly described in Sect. 1. In order to define efficient classification criteria, we first conducted an extensive examination of hundreds of events, comparing our observations with known emission types discussed in the literature and checking the consistency of our classification with the above parameters. In addition, to remove the ambiguities between Io and non-Io emissions, we used, as examples, the Io arcs shown in Leblanc (1981), Carr et al. (1983), Queinnec & Zarka (1998), which show typical shapes. Io-DAM arcs have very repeatable shapes. Conversely, non-Io emissions produce more variable patterns on the $t - f$ plane and do not exhibit a characteristic emission envelope. Therefore we focused on the arc curvature (i.e., vertex-early or vertex-late; cf. Fig. 2), together with the dominant polarization and maximum frequency. The adopted criteria are listed in Table 1.

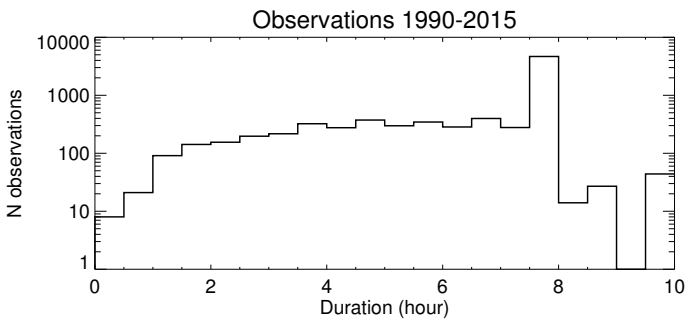
Following visual identification of an event on the dynamic spectrum corresponding to the polarization where the emission is more intense, a polygonal contour is drawn around each event (via a series of mouse clicks). Then all emission characteristics and all relevant ephemeris data at the same time resolution are computed and stored in the database (see Appendix A); the emission characteristics consist of the $t - f$ envelope at 1 min resolution, average intensity within the selected contour and in the symmetrical contour in the other polarization, fraction of points above the background within the contour, and the circular polarization ratio – Stokes V .

During the construction of the database we noticed an uncertainty on the polarization of the emission for a few observations (due to a problem in the data acquisition system; cf. Appendix A). We solved this problem by relying on the other characteristics defining each emission type and, in these particular cases only, on the occurrence in the $\text{CML} - \Phi_{\text{Io}}$ plane. As a result we estimate the fraction of emissions catalogued with an erroneous polarization in the final database to no more than 1%, as further illustrated below.

In total, 8163 observation sessions were analyzed for building the catalog, representing 54 578 h of measurements. Figure 4 shows the distribution of the durations of these observations. Each observation lasted from about 1 h (or less, exceptionally) to

Table 1. Criteria adopted in this work for cataloguing each emission type.

Emission type	Arc curvature (vertex)	Dominant circular polarization	Maximum frequency (MHz)
Io-A	late	RH	38
Io-A'	late	RH	28
Io-B	early	RH	40
Io-C	late	LH	30
Io-D	early	LH	30
non-Io-A	late	RH	38
non-Io-B	early	RH	38
non-Io-C	late	LH	32
non-Io-D	early	LH	29


Fig. 4. Distribution of the durations of daily observation sessions of Jupiter.

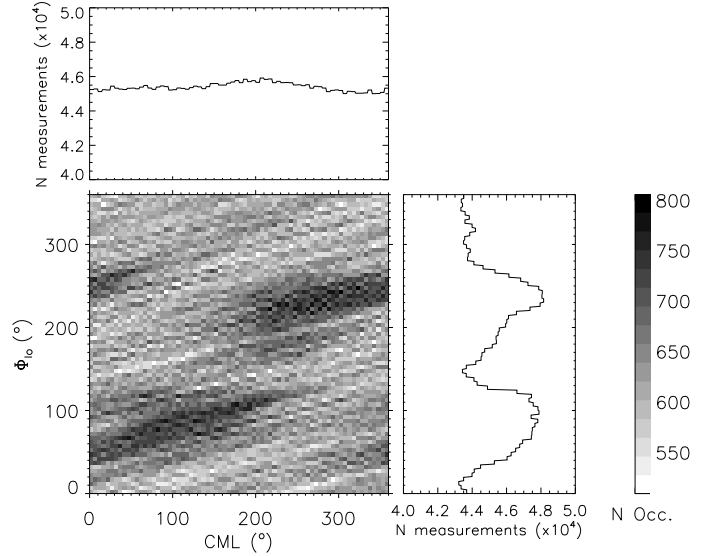
10 h, but the vast majority lasted for ~ 8 h (the standard duration of a daily routine observation). Longer observations occurred at specific occasions (e.g., the collision of debris from the comet Shoemaker-Lely 9 with Jupiter in 1994), while shorter observations depend on the competition with NDA solar observations or technical factors.

Figure 5 shows the distribution of observational time as a function of CML and Φ_{Io} . Observations were decomposed into consecutive 1-min intervals, and the figure shows the number of observational minutes occurring within $5^\circ \times 5^\circ$ bins. This number varies between 505 and 798 min across the entire plane, calculated over the whole 26-yr interval of analysis. Non-uniformity of coverage results from previous knowledge about Io emissions. Indeed, when Jupiter and the Sun are less than 8 h apart in right ascension and thus compete for NDA observation time, preference is given to Jupiter when an Io-related emission is expected to occur according to the CML– Φ_{Io} coordinates of the observer. Therefore, the coverage of Fig. 5 has higher values at the places where we expect Jupiter-Io emission to occur.

4. Analysis and results

4.1. Emission tracks in the CML– Φ_{Io} plane and overall occurrence probabilities

Figure 6 shows the emission tracks detected over the 26-yr interval studied, plotted as a function of CML and Φ_{Io} with a different color for each emission type as recorded in the catalog, together with the corresponding overall occurrence probability of the emission versus CML (top) and Φ_{Io} (right). The occurrence probability corresponds to the number of minutes of emissions


Fig. 5. Top: occurrence of observations vs. CML and Φ_{Io} over the time interval 1990–2015. The number of minutes of observations is coded in gray levels in each $5^\circ \times 5^\circ$ bin. Every bin was observed for ≥ 505 min (or 0.015% of the total duration of observations). The highest bins correspond to 798 min (0.024%) of observation and correspond to the region where we expected enhanced Io emission, which motivated a higher priority of observation. Integration of this plot vs. each dimension results in the number of minutes of observation vs. CML (top) and Φ_{Io} (right). The inhomogeneity of the coverage is $<10\%$ in both coordinates.

per 5° bin of each coordinate divided by the total duration of observations in the same bin (from the bottom left panel of Fig. 5).

Two prominent features are visible in Fig. 6. First, emission occurrence is deeply modulated by the rotation of magnetic field of Jupiter, as it varies with the CML. Broad peaks at CML values of $\sim 150^\circ$, $\sim 240^\circ$, and $\sim 320^\circ$ correspond to the known source regions A, B, and C (Io and non-Io). Second, emission occurrence is even more deeply modulated by the phase of Io. The two major peaks at $\Phi_{Io} \sim 90^\circ$ and $\sim 240^\circ$ correspond to the known Io-B/D and Io-A/A'/C emission regions, respectively (Carr et al. 1983; Genova et al. 1989).

Figure 7 is similar to Fig. 6, but here emissions are separated in Io-DAM and non-Io-DAM types. The details of differences between these two types are described in detail in Sect. 4.4. The plots demonstrate the efficiency and limitations of our cataloguing procedure relying on the classification criteria of Table 1. Non-Io-DAM emissions are clearly distinguished within Io-DAM dominated regions (right panel of Fig. 7), but they show a reduced occurrence probability in these regions (this is most prominent in Io-C), implying that some non-Io emissions are catalogued as their Io counterparts (e.g., non-Io-C \rightarrow Io-C) owing to their similar polarization and arc curvature. From the dips in the occurrence probability of non-Io-DAM at the locations of Io-DAM regions, we estimated that $\sim 10\%$ of the non-Io emissions were erroneously catalogued as their Io counterpart. Conversely, very few outliers are identified as Io emissions outside of the Io emission regions (left panel of Fig. 7), suggesting that the number of misidentifications of Io emissions is reasonably small. Overall, when compared to the total number of emissions catalogued, the fraction of misidentified emissions is thus $\sim 5\%$ and it only concerns non-Io emissions catalogued as Io emissions. The opposite case (Io emissions catalogued as non-Io emissions) is certainly $\ll 1\%$.

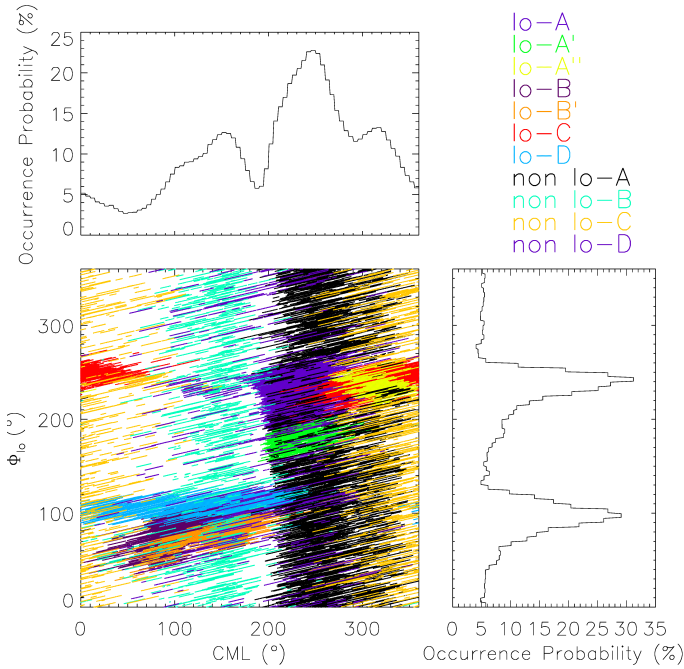


Fig. 6. Distribution of all detected emissions in the CML– Φ_{10} plane over the time interval 1990–2015 and the frequency range 10–40 MHz. In the bottom left panel, emission tracks are shown with the color code indicated in the top right. Tracks may overlap onto each other so that this figure provides qualitative information. Quantitative emission occurrence probabilities (without distinction of emission type) are plotted vs. the CML (top left) and Φ_{10} (bottom right) in 5° bins.

In Fig. 7, the well-known emission regions appear clearly. In the case of Io emissions, the two secondary peaks around $\sim 50^\circ$ and $\sim 190^\circ$ reveal new emission regions, labeled Io-A'' and Io-B'. For non-Io emission events, the faint band of purple tracks between CML $\sim 60^\circ$ and $\sim 300^\circ$ reveals another new emission region, labeled non-Io-D. In addition, the large database from which Fig. 7 is plotted results in boundaries of the emission regions in CML and Io phase somewhat different from published values (Carr et al. 1983; Bose et al. 2008). We discuss these boundaries and the three new regions in more detail below in the section presenting our analysis per emission type.

4.2. Statistics on emission intensity, duration, maximum frequency, and polarization

We analyze here the statistical distributions of four key parameters computed for each of the 6203 emission events of our database (see Appendix A), which can provide constraints to the DAM emission mechanism and scenario:

1. The average intensity is related to the emitted power; $t - f$ averaged emission intensities are only a few dB above the background in spite of the fact that individual bursts can exceed 20–30 dB because the Galactic background is bright at decameter wavelengths, the phased beam of the NDA is large ($\sim 6^\circ \times 10^\circ$), and DAM is bursty and often consists of narrow spectral bands of emission.
2. The overall emission duration results from the convolution of the source extent – in longitude and latitude and vertically along the active field lines, according to the frequency extent of the emission and the solid angle in which emission is

beamed from every point source; emission duration is also affected by intrinsic time variations of the emission.

3. The maximum frequency constrains the source location; as emission is produced at the electron cyclotron frequency along Jovian field lines, the observed maximum frequency must be lower than (or equal to) the electron cyclotron frequency at the top of Jupiter's ionosphere at the footprint of the source field line. In our catalog, maximum frequency may be slightly underestimated when signal-to-noise ratio (S/N) is low; the minimum emission frequency cannot be constrained using NDA observations due to prominent radio interference at the lowest observed frequencies and the ionospheric cutoff of the Earth at ~ 10 MHz, but it can be accessed via spacecraft measurements (e.g., Zarka et al. 2001).
4. The dominant circular polarization reveals the hemisphere of origin of the emission; a quantitative measurement of the circular polarization ratio (Stokes V , computed as explained in Appendix A), provides a finer constrain on the emission mode, mechanism, and propagation; as shown below, the determination of Stokes V from routine data is very approximate due to the low average emission intensities.

In Fig. 8 we show the distributions of average intensity (dB), duration (min.), maximum frequency (MHz), and circular polarization parameter (Stokes V) for all emission events in the catalog, and separately for Io and non-Io emissions. In Figs. 9 and 10 we show the same analysis separately for Io-DAM and non-Io-DAM. The distributions are further separated in northern and southern hemisphere sources in Fig. 9 (from the dominant circular polarization sense), and in dawn and dusk side sources in Fig. 10 (from the arc vertex; cf. Fig. 2). The corresponding numerical results are summarized in Table 2, together with occurrence probabilities for each data selection.

During the 26 yr of observations, Jovian DAM was detected 10.4% of the time. Io emissions are visible for a larger fraction of time than non-Io emissions (respectively 5.9% versus 4.5%; cf. Table 2), which confirms earlier results (Carr et al. 1983; Genova et al. 1989; Zarka 1998). However, the number of non-Io events is larger and consequently their duration is shorter. This may be because Io arcs are longer than non-Io arcs since Io arcs result from a combination of the visibility of the source (taking into account its anisotropic beaming) with the orbital motion of Io, whereas non-Io arcs result from a combination of the visibility of the source with the rotation of Jupiter of period ~ 4 times shorter than Io's orbital motion. But the source of Io emissions is a restricted set of field lines close to the Io flux tube (IFT), whereas non-Io emissions could be produced anywhere in the auroral (or even polar) regions. If non-Io emission comes from an extended source, the visibility of the source that results from the convolution of its extent in latitude and longitude with its beaming pattern (Zarka et al. 2004) would correspond to a large effective beam, which is detected as longer duration events. The fact that it is not the case suggests that non-Io emission is related to small-scale, possibly bursty auroral structures that are seen, for example, as bright spots in the UV (Prangé et al. 1998; Gérard et al. 2013), rather than as the radio counterparts of the main auroral oval as a whole. One reason for the lack of main oval radio emission may be related to the energy of precipitating electrons there (100s keV, Gérard et al. 2014; Gustin et al. 2016), which appears to be larger than optimal for the CMI. Conversely, the Io-Jupiter electrodynamic interaction appears more steady than the mechanism at the source of non-Io emissions.

The intensities of Io and non-Io emissions appear to be very close. This is not the case for the value of maximum frequencies,

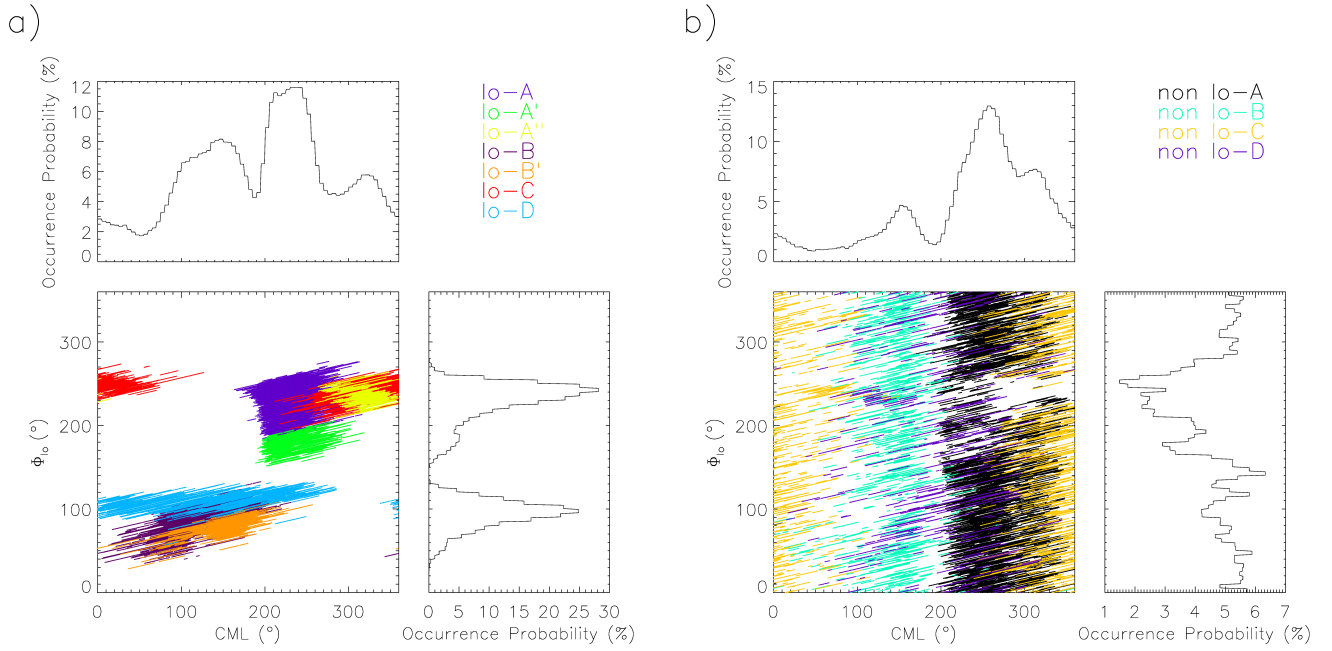


Fig. 7. Emission tracks of Io (*left*) and non-Io (*right*) emissions in the CML– Φ_{Io} plane over the time interval 1990–2015 and the frequency range 10–40 MHz, color coded as in Fig. 6. In each case, occurrence probabilities are plotted vs. the CML and Φ_{Io} in 5° bins.

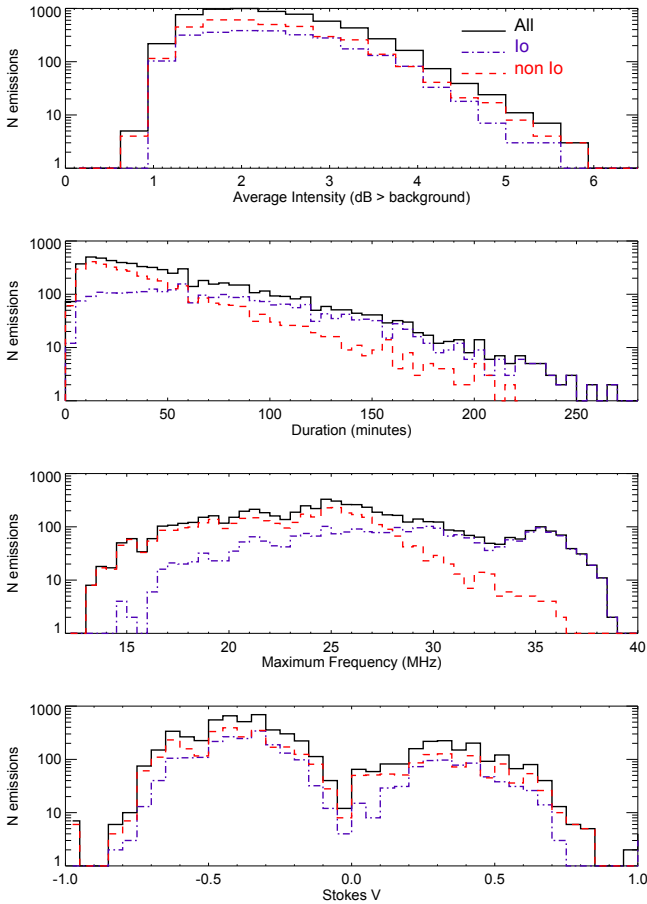


Fig. 8. Histograms of intensity, duration, maximum frequency, and circular polarization (Stokes V) for all, Io, and non-Io emissions.

which are typically higher for Io-emissions (~ 39 MHz) than for non-Io emissions. Although they may occasionally reach

~ 37 MHz, the vast majority of non-Io events have a maximum frequency of 28 MHz, as also reported by Barrow & Desch (1980). Both types of emissions have very similar distributions of circular polarization ratio, which indicates similar physical conditions for the operation of CMI in northern and southern high-latitude regions of Jupiter. The Stokes V parameter reaches marginally higher values for non-Io emissions. The most common value of $|\text{Stokes } V|$ is ~ 0.4 to 0.5 , which implies partially polarized or elliptical emission. The latter type of polarization is more likely (Dulk et al. 1992, 1994; Queinnee & Zarka 2001). We find here a more symmetrical distribution of LH and RH polarizations than discussed in these papers, but as they addressed a limited number of cases, this question needs a more in-depth study, emission type by emission type. Figure B.1 shows histograms similar to those shown in Figs. 9 and 10 for each Io and non-Io emission type.

Figure 9 analyzes the same distributions, separately for Io and non-Io emissions, further dividing emissions by hemisphere of origin (according to the emission type, A and B from the northern hemisphere, and C and D from the southern hemisphere). Northern emissions are more frequent than southern emissions. This higher northern activity might be due to stronger Pedersen currents and magnetic field amplitude in the northern hemisphere (e.g., Nichols et al. 2009), and/or to the fact that stronger magnetic field amplitude in the northern hemisphere results in more keV electrons reflected back by mirror effect, producing CMI radio emission with higher efficiency (Zarka et al. 1996). The latter suggestion is supported by the fact that the UV spot at the southern end of the IFT (or rather of the active flux tube close to the IFT) is stronger than at the northern end (Bonfond et al. 2013), thus there are more precipitated and less reflected electrons in the south. However, southern Io emissions reach higher intensities than northern emissions, which does not have a straightforward explanation in the frame of the above discussion.

For the main oval, the UV brightness is somewhat higher in the north (Clarke et al. 2009) but, as discussed above, non-Io

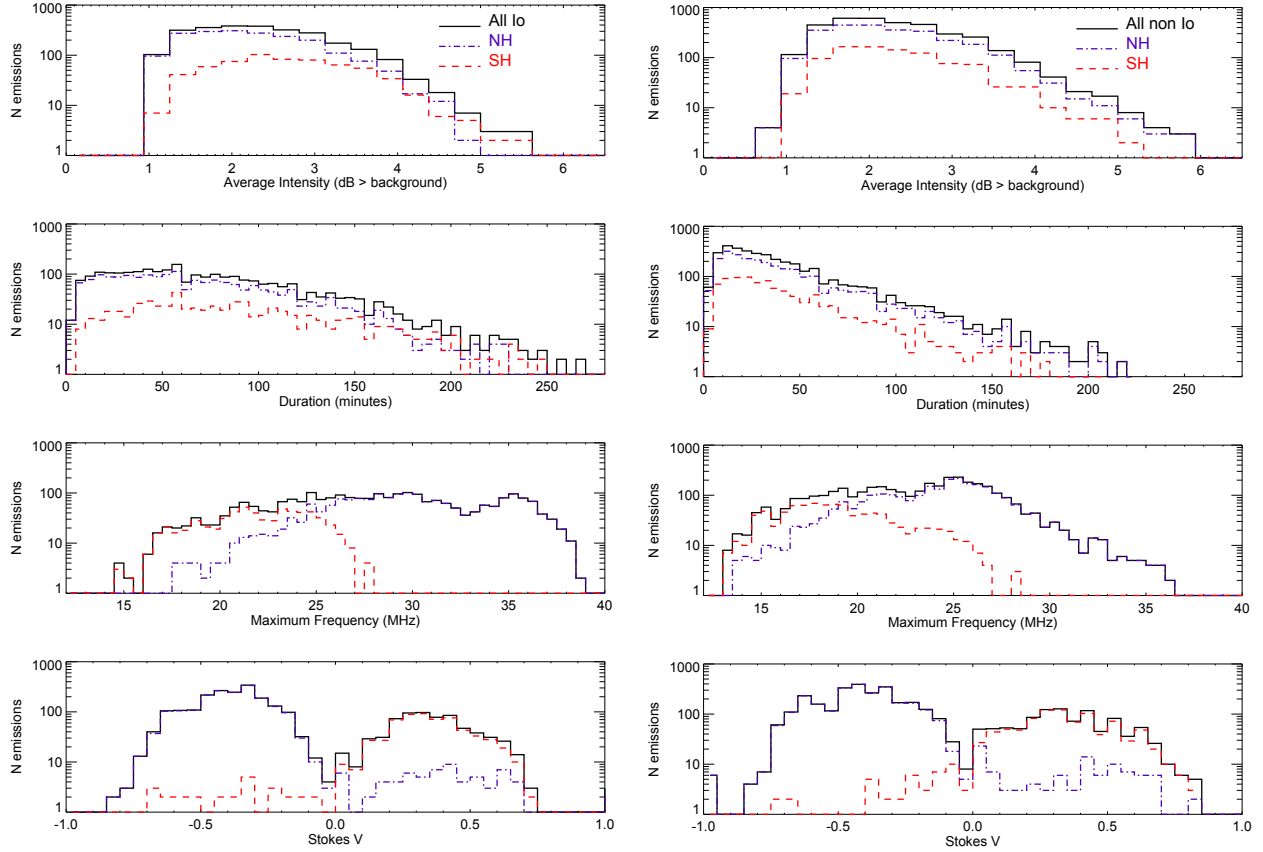


Fig. 9. Histograms of intensity, duration, maximum frequency, and circular polarization for Io (*left*) and non-Io (*right*) emissions. In each plot, histograms are also shown separately for northern hemisphere (NH) and southern hemisphere (SH) emissions.

Table 2. Statistics of emission parameters for all, Io and non-Io, northern and southern, and dawn and dusk emission events.

Type	Number of events	Total duration [hours]	Occurrence probability [%]	Intensity [dB] Avg.(Med.) $\pm\sigma$	Duration [min.] Avg.(Med.) $\pm\sigma$ Max.	Max. frequency [MHz] Avg.(Med.) $\pm\sigma$ Max.	Circular polar. (Stokes V) Avg.(Med.) $\pm\sigma$	
All events	6204	5744	10.5	2.28(2.19) \pm 0.79	55(42) \pm 44 300.	25.1(25.0) \pm 5.3 38.9	-0.20(-0.33) \pm 0.37	
All	2591	3234	5.9	2.32(2.21) \pm 0.81	74(64) \pm 49 300.	28.1(28.2) \pm 5.3 38.9	-0.20(-0.33) \pm 0.36	
NH	1958	2271	4.1	2.22(2.19) \pm 0.77	69(59) \pm 46 300.	30.1(29.8) \pm 4.2 38.9	-0.36(-0.38) \pm 0.20	
Io	SH	633	1.8	2.64(2.54) \pm 0.84	90(81) \pm 54 282.	21.9(22.0) \pm 2.8 29.4	0.32(0.33) \pm 0.21	
Dawn	1053	1409	2.6	2.38(2.26) \pm 0.87	79(68) \pm 52 300.	28.8(29.4) \pm 6.1 38.9	-0.17(-0.32) \pm 0.35	
Dusk	1538	1824	3.3	2.29(2.19) \pm 0.77	70(60) \pm 47 282.	27.6(27.9) \pm 4.6 38.6	-0.21(-0.33) \pm 0.36	
non-Io	All	3613	2511	4.6	2.23(2.19) \pm 0.78	41(30) \pm 34 222.	23.0(23.5) \pm 4.1 37.4	-0.21(-0.33) \pm 0.38
NH	2677	1847	3.4	2.21(2.18) \pm 0.78	40(30) \pm 35 222.	24.2(24.6) \pm 3.6 37.4	-0.39(-0.42) \pm 0.21	
SH	936	664	1.2	2.26(2.19) \pm 0.75	42(31) \pm 34 208.	19.1(18.7) \pm 3.0 28.5	0.31(0.33) \pm 0.21	
Dawn	954	593	1.1	2.07(1.87) \pm 0.78	36(29) \pm 29 208.	23.0(23.1) \pm 4.6 37.4	-0.18(-0.33) \pm 0.40	
Dusk	2659	1918	3.5	2.28(2.19) \pm 0.77	42(31) \pm 36 222.	22.9(23.5) \pm 3.9 35.9	-0.22(-0.33) \pm 0.36	

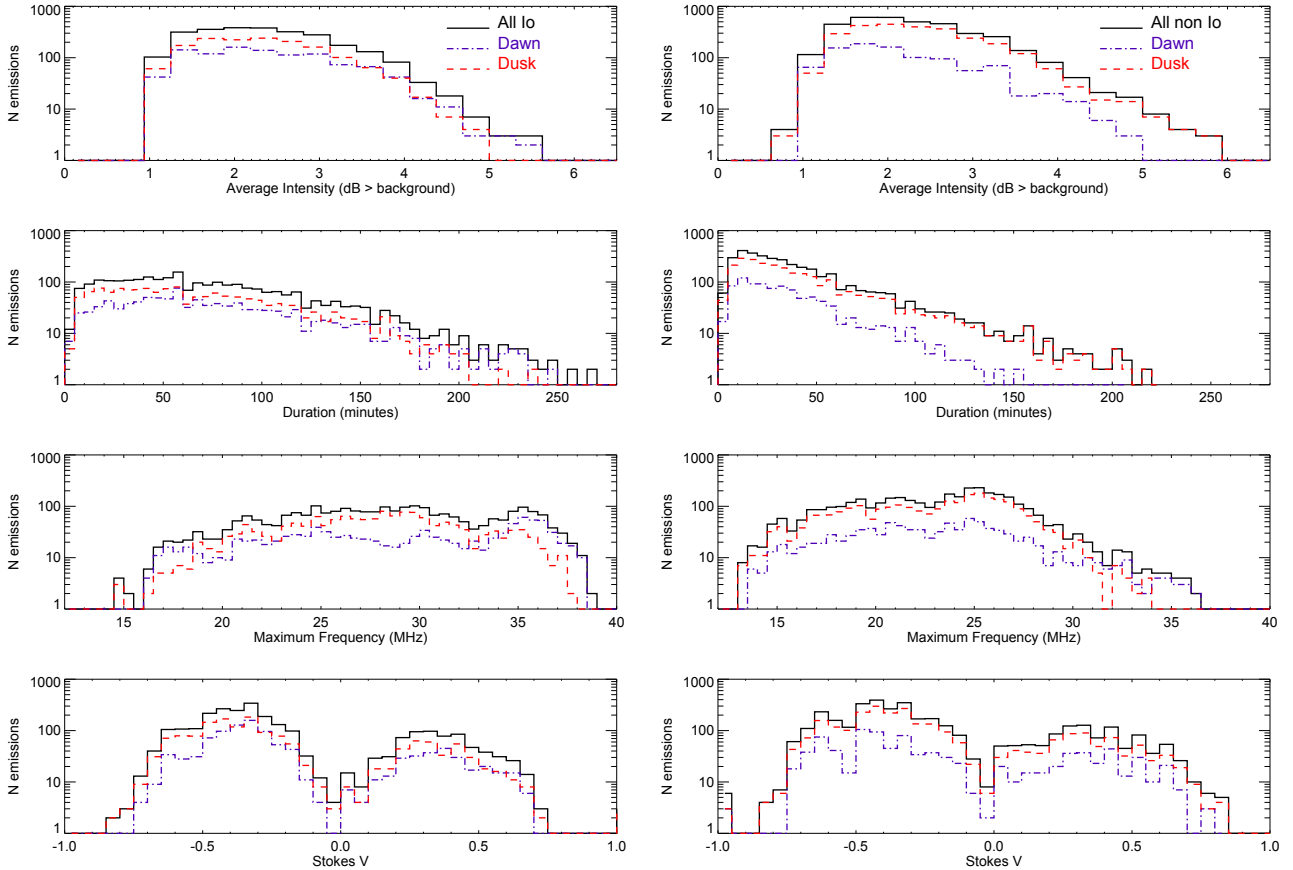


Fig. 10. Histograms of intensity, duration, maximum frequency, and circular polarization for Io (*left*) and non-Io (*right*) emissions. In each plot, histograms are also shown separately for the dawn and dusk emissions of Jupiter.

emission may be related only to hot spots along the main oval or at higher latitude. A puzzling feature of Fig. 9 is that while northern non-Io emissions are more frequent than southern emissions for all intensities and durations, northern Io emissions are more frequent than southern emissions mainly for low intensities and low durations.

Maximum frequency reaches ~ 37 MHz for non-Io emissions in the north and ~ 28.5 MHz in the south. For Io emissions, it reaches ~ 39 MHz in the north and ~ 28 MHz in the south. These high frequency limits provide strong constraints on source locations and magnetic field models (Genova & Aubier 1985; Hess et al. 2011). Emission polarization is consistent with X-mode emission: mainly RH from the north, and LH from the south. Polarization with an opposite sign is observed in $\sim 1\%$ of the detected events, which we attribute to instrumental errors (cf. Appendix A) rather than detection of O-mode, which is expected to be much weaker than X-mode (Wu 1985).

Figure 10 shows histograms for Io and non-Io emissions, separated by local time of origin according to the emission type, B and D sources corresponding to the dawn side, and A and C to the dusk side of the planet. For Io-DAM no significant difference between the dusk and dawn sides is observed. But for non-Io-DAM, dusk emissions dominate in number, intensity, and duration. The higher dusk activity might be due to emissions triggered by fast forward interplanetary shocks (FFS), as demonstrated in Hess et al. (2012) and Hess et al. (2014). These authors showed that FFS-triggered DAM emissions onset in the afternoon sector and suggested that the relatively empty cushion on the dawn side of the magnetosphere of Jupiter absorbs FFS-triggered compressions, whereas dusk emissions were favored

by compressions of the thick current sheet on that side of the planet (Kivelson & Southwood 2005), possibly heating the plasma via viscous interaction or adiabatic compression.

It has been also noted from the histograms that the highest observed maximum frequencies of DAM events are slightly higher on the dawn side than on the dusk side. Distributions of Stokes V are similar for Io and non-Io emissions and for dawn and dusk sources.

The properties deduced from histograms characterize the emission properties averaged over a long time, possibly mixing competing physical effects. A more detailed analysis, in the context of our present knowledge of radio and UV emissions from Jupiter’s aurora and Jupiter-Io interaction, must take into account the temporal variations of the parameters studied, which may depend on the solar wind fluctuations, seasonal variations of the ionospheric conductivity, the volcanic outbursts of Io, and the way all these fluctuations affect the solar wind-magnetosphere-ionosphere-satellite couplings and consequently the magnetospheric activity. The study of these time variations is made possible using our catalog, and it will be the subject of a future paper.

4.3. Distributions versus central meridian longitude and Io longitude

Another way of considering the variations of the four key parameters defined above is to plot them as a function of the periodic coordinate that may affect emission generation and visibility.

In the case of Io emissions, this coordinate is the Jovicentric longitude of Io (Λ_{Io} where $\Lambda_{\text{Io}} = \text{CML} - \Phi_{\text{Io}} + 180^\circ$; see Fig. 1), i.e., the position of the satellite in the rotating Jovian magnetic

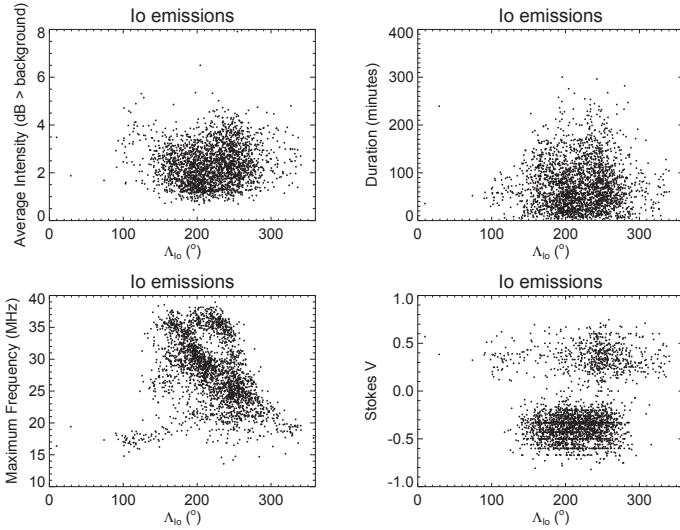


Fig. 11. Intensity, duration, maximum frequency, and polarization ratio of Io emissions as a function of Λ_{Io} . A single point is plotted per emission event (i.e., the average intensity or polarization over the event, its duration, and the maximum frequency reached during the emission event). The abscissa is the longitude of Io at the midpoint – in time – of the event.

field, which modulates the Alfvénic current intensity, the Alfvén wave topology (e.g., Saur et al. 2004), and the maximum frequency at the foot of the active field line. The corresponding plots are shown in Fig. 11. They show that (i) Io emissions are mainly detected for $90^\circ \leq \Lambda_{\text{Io}} \leq 340^\circ$; (ii) this range is even more restricted in the northern hemisphere ($120^\circ \leq \Lambda_{\text{Io}} \leq 290^\circ$; Fig. 11, bottom right panel); and (iii) the distribution of maximum frequencies is well structured versus Λ_{Io} (Fig. 11, bottom left). This structure is discussed in more detail below.

In the case of non-Io emissions, the periodic coordinate is the CML, which is related to the longitude of dawn and dusk sources via their beaming angle. The corresponding plots are shown in Fig. 12. One can recognize easily the emission regions from Fig. 7b (especially A, B, and C) as separate densely populated groups of points, and the quasi-absence of emissions for $180^\circ \leq \text{CML} \leq 200^\circ$. Non-Io-A emissions have the highest intensity and longest duration (albeit with a large scattering) surrounded by non-Io-B and non-Io-C emissions. The A and B emissions, well identified as the RH (Stokes $V < 0$) blobs on the bottom right panel in restricted CML ranges, reach maximum frequencies above 30 MHz in similarly restricted CML ranges ($\sim 220^\circ$ – 300° and $\sim 80^\circ$ – 180° , respectively). This can be interpreted as the passage of a single source region near the dusk side and the dawn side limbs, respectively. Elementary 2D geometry suggests that the source lies at the midpoint of the above CML ranges, i.e., $\sim 195^\circ$, located on the negative gradient (downward slope) of the strong magnetic field anomaly in the northern hemisphere of Jupiter relative to the rotation of the planet (Hess et al. 2011). Along such a negative gradient (where $d|B|/d\text{CML} < 0$), part of the electron population mirroring on the magnetic anomaly now precipitates deeper because it is eventually lost by collisions and generates a loss cone that can drive radio wave generation by the CMI. With a source at $\sim 195^\circ$, the center of the above CML ranges implies an emission beamed at $\sim 65^\circ$ from the magnetic field of the source, which is consistent with the CMI prediction of widely open hollow cone beams. Of course the problem must be studied in 3D geometry, and the non-Io sources are extended or rather spread over a broad longitude

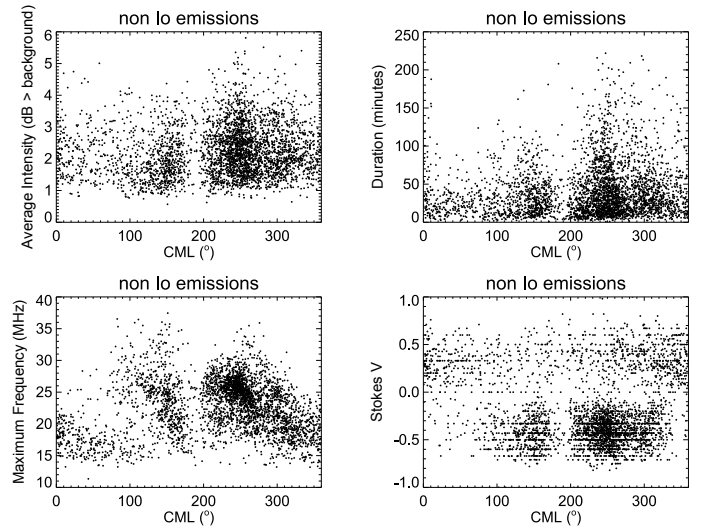


Fig. 12. Intensity, duration, maximum frequency, and polarization ratio of non-Io emissions as a function of CML. As for Fig. 11, a single point is plotted per emission event at the CML midpoint of the event.

range, so that the above values are only indicative. In the southern hemisphere, LH (Stokes $V > 0$) non-Io emissions are more uniformly spread at all values of CML, and their maximum frequency is lower. This is consistent with the weaker and more uniform magnetic field in southern hemisphere of Jupiter without any magnetic anomaly comparable to the northern hemisphere.

For Io and non-Io emissions, scatter plots of any of the above four key parameters against any other one do not show any significant trend, suggesting that the histograms of Figs. 8 to 10 and the scatter plots in Figs. 11 and 12 illustrate well the main statistical properties of these emissions.

Figure 13 focuses on the distribution of maximum frequencies of Io and non-Io emissions similar to the bottom left panels of Figs. 11 and 12, but with two major differences: each emission type is color coded as in Figs. 6 and 7, and instead of a single point per emission event, the complete variation of the maximum frequency during each event is depicted at the time resolution of 1 min. The plots are thus more densely populated and more accurate. Figure 13a depicts the maximum frequency versus the CML for Io emissions, showing that Io-A and Io-B emissions reach the highest frequencies (up to 39 MHz) and demonstrating clearly the distinct natures of Io-A' and Io-C emissions (and to a lesser extent of Io-B and Io-B' emissions). Figure 13b reveals clearly the non-Io-D emission. Figure 13c shows more convincingly than Fig. 11 that Io emissions cluster in a limited range of Io's longitude ($\sim 120^\circ$ – 300° for northern sources and $\sim 70^\circ$ – 360° for southern sources), with an envelope that draws an overall high-frequency limit as a function of Λ_{Io} . This envelope imposes a strong constraint on the magnetic field model and the lead angle of the active field line close to the IFT (Genova & Aubier 1985; Zarka et al. 2002; Hess et al. 2011). Figures 13c–e also emphasize the differences in the various Io-DAM emission types, which can have distinct maximum frequency envelopes at the same Λ_{Io} . As the clouds of points of several Io-DAM emission types are superimposed in Fig. 13c and mask each other, Figs. 13d, e depict the same measurements as Fig. 13c but with different emission types plotted at the foreground. Finally, Fig. 13f shows the non-Io emissions versus Λ_{Io} and, as expected, no modulation in Λ_{Io} seems to be present, except the lack of points around 230° that corresponds to the gap at the Io-A/C phase on Fig. 7b. It

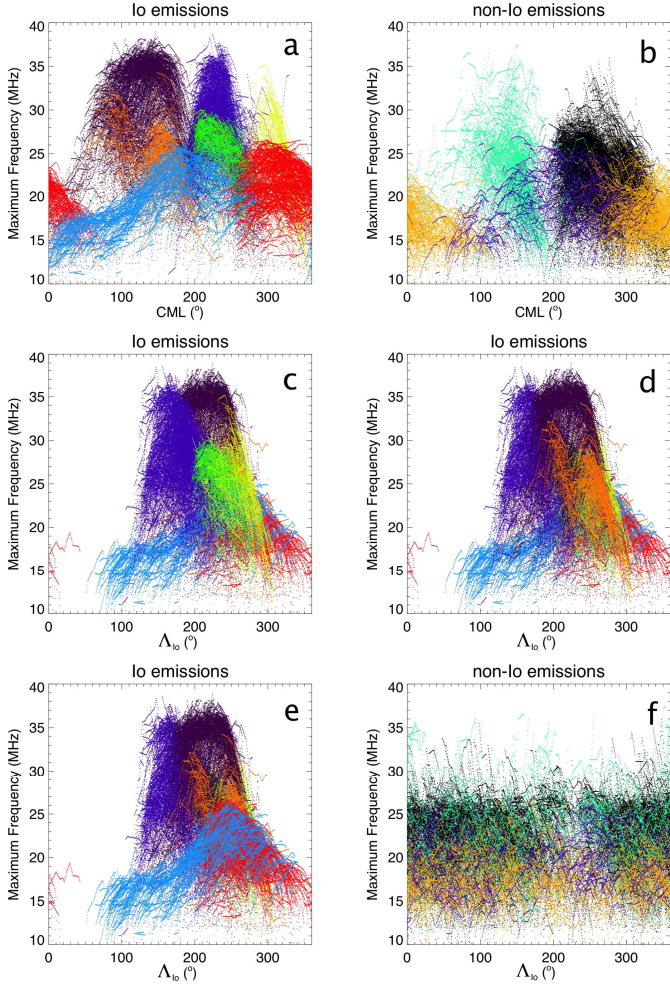


Fig. 13. Maximum frequency envelopes of Io and non-Io emissions at the time resolution of 1 min: **a)** for Io emissions as a function of CML; **b)** for non-Io emissions as a function of CML; **c)–e)** for non-Io emissions as a function of Λ_{Io} (these 3 panels differ only by which emission types are plotted on the foreground, so that they are complementary); and **f)** for non-Io emissions as a function of Λ_{Io} . The color code is the same as in Figs. 6 and 7.

also provides an alternative view on the dependencies of maximum emission frequency on Λ_{Io} shown in the third row of Fig. 9 where RH (northern) and LH (southern) maximum frequencies reach ~ 36 MHz and ~ 27 MHz, respectively.

4.4. Analysis per emission type

Figures 14 and 15 show examples of dynamic spectra of all DAM emission types for Io and non-Io sources each in its dominant polarization, respectively. Table 3 lists statistical values of the same emission parameters as in Table 2, but in Table 3 these values are separated by emission type.

Io-A emission characteristics derived here are consistent with previously published characteristics (Carr et al. 1983; Genova et al. 1989; Queindec & Zarka 1998; Hess et al. 2008a). This is mainly observed within $CML = 180^\circ\text{--}310^\circ$ and $\Phi_{\text{Io}} = 180^\circ\text{--}280^\circ$. Io-A events are composed of multiple vertex late arc structures with RH dominant polarization, average duration of 71 min, and maximum frequency of 38.6 MHz. Io-A' events are also composed of vertex late arcs (also RH), but these events have very weak curvature in the $t - f$ plane (Leblanc 1981)

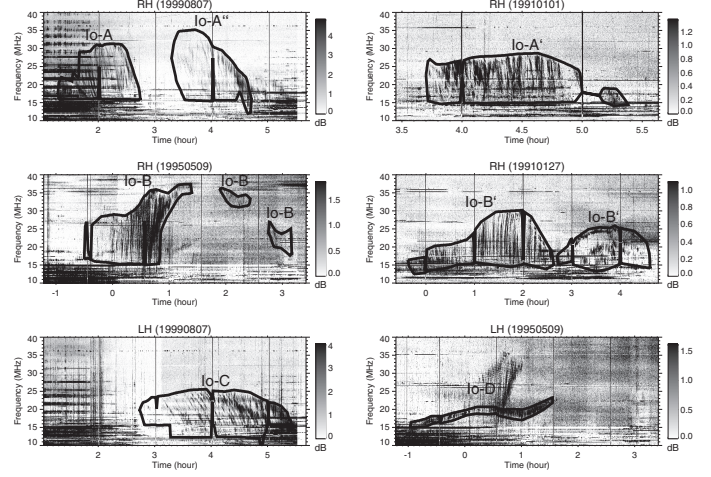


Fig. 14. Dynamic spectra of typical Io-DAM arcs. The entire frequency range (10–40 MHz) is shown. The circular polarization and the date (YYYYMMDD) are indicated on the top of each plot. Abscissa is the time (hours UT) of that day (see the convention for date and time in the caption of Fig. 3). The intensity scale (increasing darkness) is in dB above the background to the right of each plot. Each emission component is identified by a thick polygonal contour and the corresponding emission type above it. Dark vertical lines separated by one hour are calibration sequences (see Sect. 2 and Fig. 3). We selected examples with typical shapes in the $t - f$ plane. In some cases (19950509, 19990807), different RH and LH emissions are detected on the same day and overlap in time, each appearing dominant in the dynamic spectrum of corresponding polarization.

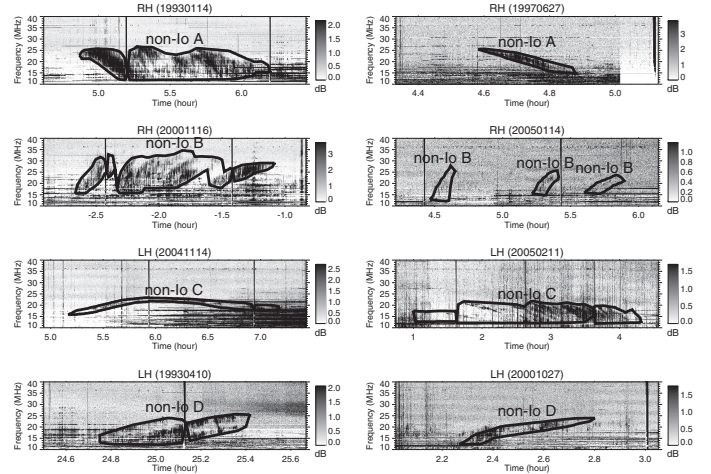


Fig. 15. Same as Fig. 14, but for non-Io emissions.

and cover the range $CML = 190^\circ\text{--}300^\circ$ and $\Phi_{\text{Io}} = 150^\circ\text{--}200^\circ$. They exhibit a maximum frequency of 33.4 MHz, which is higher than the value given in Carr et al. (1983). Our classification criteria allowed us to identify a new emission type with unique spectral characteristics, covering a specific area of the $CML - \Phi_{\text{Io}}$ plane. The emission often exhibits only one vertex late arc with RH dominant polarization, maximum frequency up to 35.2 MHz, and an average duration of 50 min. We observed it within $CML = 270^\circ\text{--}360^\circ$ and $\Phi_{\text{Io}} = 210^\circ\text{--}270^\circ$, overlapping with Io-C. This vertex-late arc was previously described as “Io-C RH” by Boudjada et al. (1995), who suggested that emissions of this type originate from the same source in the same hemisphere as Io-C. But this suggestion appears to be incompatible with the commonly accepted CMI-based theoretical modeling by

Table 3. Statistics of emission parameters per emission type.

Type	Number of events	Total duration [h]	Occurrence probability [%]	Intensity [dB]	Duration [min.]	Max. frequency [MHz]	Circular polar. (Stokes V)	
				Avg.(Med.) $\pm \sigma$	Avg.(Med.) $\pm \sigma$ Max.	Avg.(Med.) $\pm \sigma$ Max.	Avg.(Med.) $\pm \sigma$	
A	771	922	1.68	2.15(2.16) \pm 0.66	71(66) \pm 43 224.	30.4(30.4) \pm 3.6 38.6	-0.37(-0.40) \pm 0.22	
A'	249	200	0.37	2.08(1.94) \pm 0.75	47(39) \pm 36 180.	26.8(27.2) \pm 2.3 33.4	-0.39(-0.43) \pm 0.20	
A''	150	134	0.25	2.23(2.19) \pm 0.70	52(51) \pm 27 136.	27.7(27.8) \pm 3.2 35.2	-0.35(-0.37) \pm 0.22	
Io-	B	611	795	1.46	2.31(2.19) \pm 0.89	77(65) \pm 53 300.	32.9(34.3) \pm 3.8 38.9	-0.34(-0.35) \pm 0.18
	B'	177	221	0.40	2.25(2.37) \pm 0.79	74(63) \pm 49 258.	26.0(26.0) \pm 3.2 34.3	-0.35(-0.37) \pm 0.18
	C	368	569	1.04	2.76(2.69) \pm 0.83	92(81) \pm 56 282.	22.2(22.2) \pm 2.6 29.4	0.30(0.32) \pm 0.21
	D	265	394	0.72	2.49(2.39) \pm 0.84	88(81) \pm 51 249.	21.5(21.6) \pm 2.9 27.9	0.34(0.36) \pm 0.21
	A	2012	1474	2.70	2.31(2.19) \pm 0.78	43(32) \pm 37 222.	24.2(24.8) \pm 3.2 35.9	-0.38(-0.41) \pm 0.22
non-Io-	B	665	373	0.68	1.94(1.87) \pm 0.74	33(26) \pm 25 173.	24.2(24.4) \pm 4.5 37.4	-0.41(-0.43) \pm 0.20
	C	647	444	0.81	2.21(2.19) \pm 0.73	40(29) \pm 34 200.	18.5(18.3) \pm 2.7 28.0	0.30(0.32) \pm 0.21
	D	289	220	0.40	2.36(2.21) \pm 0.79	45(35) \pm 34 208.	20.2(20.3) \pm 3.4 28.5	0.35(0.35) \pm 0.19

Hess et al. (2008a), so we concluded that it is an emission coming from the northern hemisphere and we called this newly identified emission type Io-A''. We show a representative example of an Io-A'' event following an Io-A one in the top left spectrogram of Fig. 14. In Figs. 13c and B.2 (top left), we note that Io-A' and Io-A'' correspond to the same ranges of Λ_{Io} and maximum frequency that is distinct from those of Io-A emission. Furthermore, all four key parameters listed in Table 3 and shown in Fig. B.1 (left column) are very similar for Io-A' and Io-A'' emissions and different for Io-A emissions. This points to a different physical source, possibly the same for Io-A' and Io-A'' emissions (albeit they have different $t - f$ morphologies as shown on Fig. 14 (top row)) that are distinct from the source of Io-A emissions.

Io-B emission displays two types of morphology. The classical Io-B great arc with precursor fringes and a long $t - f$ tail has been described by Carr et al. (1983) and studied in detail by Queinnee & Zarka (1998). It is RH polarized and we find here an average duration of 77 min for its main part (see Fig. 14, middle-left, and Table 3). Figures 6 and 7 show that the Io-B emission region starts at lower CML than previously thought. It reaches a maximum frequency ~ 38.9 MHz, slightly below the value derived from Voyager observations (Carr et al. 1983). These differences can be attributed to the different sensitivities (and thus S/N) of Earth-based and Voyager observations and to the different Jovicentric latitudes of the observers. The latter parameter appears to have a strong impact on the measured emission properties (Barrow 1981; Garcia 1996; Imai et al. 2011a), which will deserve a dedicated study. Below the Io-B emission region (i.e., at lower values of Φ_{Io}) we often noticed a series of narrowband (typically 1–2 MHz) emissions with $t - f$ characteristics that are different from Io-B that we labeled Io-B'. This emission generally consists of two consecutive groups of vertex early arcs, such as the example shown in Fig. 14 (middle-right).

Both groups have similar $t - f$ envelopes with a maximum frequency up to 34.3 MHz and dominant RH polarization. Leblanc (1981) has already identified and discussed possible subtypes of Io-B emissions in Voyager observations, and Clarke et al. (2014) have discussed one similar case that they observed in the same CML- Φ_{Io} region. Wright & Smith (1990) suggested, via theoretical modeling, that low-frequency oscillations of the Jovian magnetic field lines disturbed by Io could account for the apparent splitting of the Io-B source region into two components. Figures 13d and B.2 (top right) show that the Io-B' emission has a double-peak structure in maximum frequency versus Λ_{Io} , suggesting a possible further subdivision in Io-B' and Io-B'' types.

Figures 6 and 7 indicate the Io-C emission starts before the CML = 280° mentioned in (Carr et al. 1983). This has also been noted by Clarke et al. (2014) in their analysis of a single Io-C event. However, as discussed below in Table 4, the extension of the Io-C region to CML < 270° (down to CML $\sim 240^\circ$) corresponds to occurrence probabilities <10%. The Io-C emission is predominantly LH polarized, made of vertex late arcs, and it has the highest average intensity of all Io emissions (cf. Table 3). The average duration is 1.5 h and maximum frequency reaches 29.4 MHz. This is much lower than the 36 MHz value noted by Carr et al. (1983). This is because we introduced the new type A'' for RH events and removed these A'' events from the statistical analysis of Io-C events.

The Io-D emission is typically composed of a single vertex early arc with a maximum frequency up to 27.9 MHz (Fig. 14, bottom-right). This maximum frequency is much higher than the 18 MHz mentioned in Carr et al. (1983), and corroborates statistically the example shown in Queinnee & Zarka (1998) and modeled in Hess et al. (2008a). Io-D emission is predominantly LH polarized and may last up to 1.5 h as well. This emission has been detected up to CML values larger than 200°, and the new

Table 4. CML– Φ_{10} range of Io emissions for three occurrence probability thresholds (when applicable).

Type	10% occurrence		25% occurrence		50% occurrence	
	CML range (°)	Φ_{10} range (°)	CML range (°)	Φ_{10} range (°)	CML range (°)	Φ_{10} range (°)
Io-A	185–275	185–265	190–260	195–260	210–255	225–245
Io-A'	200–265	160–195				
Io-A''	300–345	220–245				
Io-B	75–200	55–115	95–185	80–110	116–165	85–105
Io-B'	130–185	65–95	285–360	230–255		
Io-C	270–45	215–260	285–360	230–255		
Io-D	20–230	95–125				

Notes. The limits listed correspond to overall rectangular boxes.

boundaries of Io-D are listed in Table 4. The values in Table 3 support the histogram of Fig. 9, i.e., southern Io emissions often reach higher intensities than northern Io emissions.

Non-Io emissions have $t - f$ envelopes less extended than Io emissions, i.e., few events exceed ~ 28 MHz; they may reach ~ 37 MHz in the northern hemisphere (cf. Table 3 and Fig. 15). But the arc shapes of all DAM events are repeatable and recognizable enough to allow us to separate to a large extent Io and non-Io emissions overlapping in the CML– Φ_{10} plane (Fig. 7). With our new database, the CML boundaries of non-Io emissions have been modified when compared to previous studies (Carr et al. 1983; Genova et al. 1989). They are listed in Table 5. For example, non-Io-C starts at CML = 255° (and even down to $\sim 240^\circ$ at very low occurrence level) and ends at CML = 95° (up to $\sim 140^\circ$ at very low occurrence level). The maximum frequency of non-Io-C (28 MHz) is also lower than previously thought for the same reason as Io-C (identification and removal of embedded Io-A'' emissions).

Non-Io-A emissions have maximum frequencies of 35.9 MHz, which is very consistent with the literature. Non-Io-A events are by far the most numerous. They include a “zoo” of various arc types (Fig. 15, top row) that are possibly from different elementary sources; these sources may include emissions induced by satellites other than Io that have not been identified until now. Those are under study and will be the subject of a future paper. Non-Io-B have the highest maximum frequency among non-Io emissions (37.4 MHz), which is also consistent with the literature, and the strongest circular polarization of all DAM emissions (cf. Table 3 and Queindec & Zarka 2001).

We identified around 289 events ($\sim 0.4\%$ occurrence) with LH polarization, vertex early arcs, and maximum frequency about 28.5 MHz, distributed over a very broad range of CML ($10^\circ - 340^\circ$) for all Φ_{10} (see detailed limits in Table 5). This new emission type has all the required characteristics for being identified as the non-Io-D emission. Actually the review by Bose et al. (2008) mentioned a non-Io-D emission within the CML range $\sim 0^\circ - 200^\circ$, but without any supporting observation. Imai et al. (2011b) also proposed the identification of a non-Io-D emission in a diagram of the occurrence probability of non-Io-DAM built from Cassini observations of Jupiter in 2001, but this emission appears in a restricted range of CML ($40^\circ - 60^\circ$) and frequency (7–11 MHz). The large statistical basis of our catalog allows us to identify unambiguously and characterize this emission type, which is much less frequent than the others and is diluted over a broad range of CML overlapping with that of other non-Io emission types.

Figure 16 indicates the occurrence probability as a function of CML and Φ_{10} for each Io emission type. This probability is obtained by dividing the total duration of the events of a given

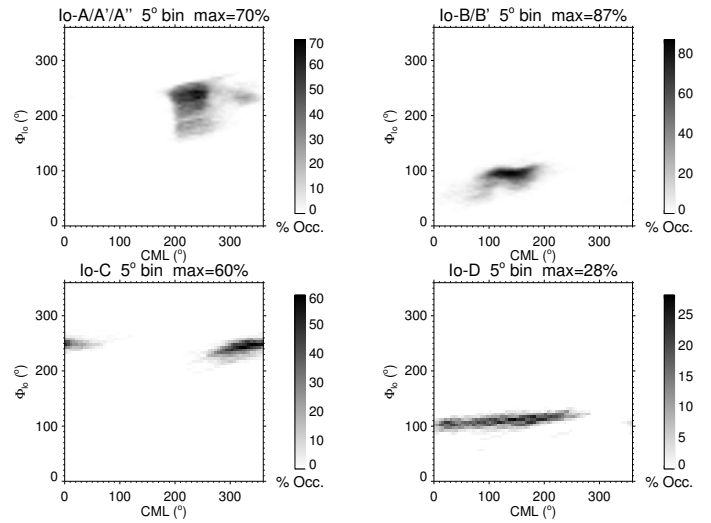


Fig. 16. Occurrence probability of Io emissions vs. CML and Φ_{10} , within 5° bins, in gray-shaded scale. Maximum probability (in %) is indicated at the top of each panel. Emission types (A, A', A''), originating from the same hemisphere and planetary limb, are grouped in one panel. The same is true for emission types (B, B').

Table 5. CML range of non-Io emissions, corresponding to a level of 10% of the maximum integrated occurrence probability vs. the CML.

Type	CML min. (°)	CML max. (°)
Non-Io-A	200	340
Non-Io-B	80	190
Non-Io-C	255	95
Non-Io-D	55	325

type that occur in a $5^\circ \times 5^\circ$ bin of the CML– Φ_{10} plane by the total observational time in that bin as depicted in Fig. 5. Io emissions are grouped by hemisphere and limb position and maximum probability (in %) is indicated at the top of each plot in Fig. 16. Northern hemisphere emissions reach very high occurrence probabilities in restricted areas. Table 4 gives the overall limits in CML and Φ_{10} , for each emission type, corresponding to an occurrence probability $\geq 10\%$, 25% , and 50% , where occurrence reaches high enough values.

Figure 17 and Table 5 provide similar information for non-Io emissions. As their occurrence probability is generally lower, Table 5 lists the minimum and maximum CML value of each non-Io region (without any dependence in Φ_{10} of course) determined from its integrated occurrence versus the CML.

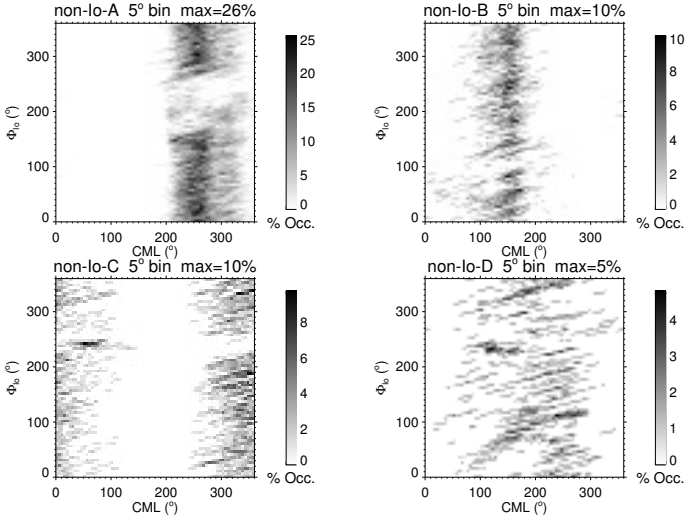


Fig. 17. Occurrence probability of non-Io emissions vs. CML and Φ_{Io} .

5. Discussion and perspectives

We have built a database of 26 yr of observations of the DAM emission conducted by the NDA, using new criteria for the event classification into Io and non-Io emission types (Table 1). The cataloging of the DAM events was performed in a way that allowed us to record extensive information on each emission (Appendix A). Our approach is a more elaborate version of the catalogs by Thieman (1979), Leblanc et al. (1981, 1983, 1989, 1990, 1993), as our database covers a longer time interval (the longest interval on Jovian DAM ever studied at once) and contains much more detail on the emission than previous catalogs. It is a different approach from the construction of occurrence probability diagrams from spacecraft observations, by stacking observations, for example, as a function of CML and frequency, in which the detected signal exceeds a certain threshold (Higgins et al. 1999; Imai et al. 2008, 2011b). In the latter case, the data must be reasonably interference-free (which is not the case for ground-based data), and it is often limited to low frequencies (5.6 MHz for Galileo, 16.1 MHz for Cassini, but 40 MHz for Voyager). But in our approach, the morphology of each emission event is recognized and classified, and all data about each emission event is stored in the database and can be further exploited through statistical analyses, for example, separately for each emission type.

We carried out a first statistical analysis of our database, focusing on occurrence rates, intensity, duration, maximum frequency and polarization of the events. This study suggests a number of results listed below, the confirmation of which will motivate specific in-depth analyses:

1. Non-Io-DAM appears to be related to small-scale, possibly bursty auroral structures.
2. Northern emissions are more frequent but southern emissions are more intense.
3. In the case of Io emissions, the excess of northern events specifically concerns low intensity and low duration emissions.
4. In the case of non-Io emissions, dusk emissions dominate dawn emissions by occurrence, intensity, and duration.
5. The distribution of non-Io emissions versus the CML suggests that radio sources are preferably located above auroral regions, where $d|B|/dCML < 0$.

6. The distribution of the maximum frequency of Io emissions is densely clustered versus Io's longitude Λ_{Io} ; its $t - f$ envelope imposes a strong constraint on the Io-Jupiter interaction mechanism (lead angle), provided that the Jovian internal – and surface – magnetic field is well-known.

The results obtained for each emission type are generally in good agreement with previous works, but a few new results can be highlighted:

- Two new Io-induced radio emission types were discovered or identified: Io-A' and Io-B', which have spectral characteristics distinct of other emission types.
- The CML– Φ_{Io} contours and maximum frequency of known emission types, especially Io-C and Io-D, are redefined (differently from the values in the literature); Io-C is detected at lower CML, has a maximum frequency ~ 29 MHz, and exclusively LH polarization; Io-D is observed beyond published limits and has a maximum frequency that is higher than described in previous works.
- The non-Io-D type was identified in a broad CML range (and all Io phases), with LH polarization, maximum frequency ~ 28 MHz, and low occurrence probability.

These new results are due to the exceptional length of the database, the digital data format, the new classification method adopted (with a set of consistent, minimum, necessary, and sufficient criteria), and the care and accuracy in the application of these criteria for building the database.

We believe that the present paper will provide a support for future theoretical studies of Jovian DAM phenomenology. For example, it can stimulate further attempts to predict theoretically the Io-DAM occurrence within specific regions on the CML– Φ_{Io} plane (Galopeau et al. 2004, 2007). It can also be used for testing the explanation proposed by (Wright & Smith 1990) for the apparent splitting of Io-A or Io-B source regions into two or more components in terms of oscillations of the Jovian magnetic field lines disturbed by Io. We hope that the detailed plots and tables presenting, for example, the occurrence probability for each emission type (Figs. 16 and 17, Tables 4 and 5), will provide a reliable basis for future observations by professional and amateur radio astronomers (e.g., Cecconi et al. 2015), whereas the general statistics of Figs. 6–13 and the emission events morphology of Figs. 14 and 15 will provide a framework for the study of Jovian DAM with the Juno mission (Bagenal et al. 2014) and for reanalyses of past spacecraft observations (Voyager, Cassini). In particular, one of the major outcomes of the Juno mission should be a near-perfect Jovian internal field model, which will remove all uncertainty on the surface magnetic field and provide a new and accurate frame for the analysis and interpretation of data from our database. For example, variations of the maximum frequency will directly give an estimate for the lead angle of the active field line versus Λ_{Io} and therefore allow us to measure the radio beaming angle of Io emissions accurately. Finally, the present database will be the support of several further papers. Those include the control of Jovian DAM emissions by other satellites (in addition to Io), long-term variations of the emissions occurrence (e.g., with Earth's Jovicentric latitude or season), or the solar wind influence on the outer Jovian magnetosphere.

Acknowledgements. M.S.M. acknowledges the support from CNPq projects 201740/2014-1-SWE, 14314/2014-8-GM/GD and 154763/2016-0-PDJ, Brazil. E.E. acknowledges the research support project CNPq/PQ 302583/2015-7, Brazil. M.V.A. acknowledges the research support project CNPq/PQ 305373/2010-2, Brazil. Part of this work has been carried out within the

LABEX Plas@par project, and received financial state aid managed by the Agence Nationale de la Recherche, as part of the programme “Investissements d’avenir” under the reference ANR-11-IDEX-0004-02. The Nançay Radioastronomy Station acknowledges the support of the Conseil Régional of the Région Centre in France. The Nançay Decameter Array acknowledges the support from the Programme National de Planétologie and the Programme National Soleil-Terre of CNRS-INSU.

References

- Bagenal, F., Adriani, A., Allegrini, F., et al. 2014, *Space Sci. Rev.*, **4**
- Barrow, C. H. 1981, *A&A*, **101**, 142
- Barrow, C. H., & Desch, M. D. 1980, *A&A*, **86**, 339
- Bigg, E. K. 1964, *Nature*, **203**, 1008
- Boischot, A., & Aubier, M. G. 1981, *J. Geophys. Res.*, **86**, 8561
- Boischot, A., Rosolen, C., Aubier, M. G., et al. 1980, *Icarus*, **43**, 399
- Bonfond, B., Hess, S., Gérard, J.-C., et al. 2013, *Planet. Space Sci.*, **88**, 64
- Bose, S. K., Sarkar, S., & Bhattacharyya, A. B. 2008, *Indian J. Radio Space Phys.*, **37**, 77
- Boudjada, M. Y., Rucker, H. O., & Ladreiter, P. H. 1995, *A&A*, **303**, 255
- Burke, B. F., & Franklin, K. L. 1955, *J. Geophys. Res.*, **60**, 213
- Carr, T. D., Desch, M. D., & Alexander, J. K. 1983, Phenomenology of magnetospheric radio emissions, ed. A. J. Dessler, 226
- Cecconi, B., Hess, S. L. G., Le Sidaner, P., et al. 2015, *European Planetary Science Congress, 27 Sep. – 2 Oct. 2015, Nantes, France*, id. EPSC2015-140, Online at <http://meetingorganizer.copernicus.org/EPSC2015>, 10, EPSC2015
- Clarke, J. T., Nichols, J., Gérard, J.-C., et al. 2009, *J. Geophys. Res. (Space Phys.)*, **114**, A05210
- Clarke, T. E., Higgins, C. A., Skarda, J., et al. 2014, *J. Geophys. Res. (Space Phys.)*, **119**, 9508
- Dulk, G. A., Lecacheux, A., & Leblanc, Y. 1992, *A&A*, **253**, 292
- Dulk, G. A., Leblanc, Y., & Lecacheux, A. 1994, *A&A*, **286**, 683
- Gallet, R. M. 1961, Radio Observations of Jupiter. II, eds. G. P. Kuiper, & B. M. Middlehurst, 500
- Galopeau, P. H. M., Boudjada, M. Y., & Rucker, H. O. 2004, *J. Geophys. Res. (Space Phys.)*, **109**, A12217
- Galopeau, P. H. M., Boudjada, M. Y., & Rucker, H. O. 2007, *J. Geophys. Res. (Space Phys.)*, **112**, A04211
- Garcia, L. 1996, Ph.D. Thesis, University of Florida, Gainesville
- Genova, F., & Aubier, M. G. 1985, *A&A*, **150**, 139
- Genova, F., Aubier, M. G., & Lecacheux, A. 1981, *A&A*, **104**, 229
- Genova, F., Zarka, P., & Lecacheux, A. 1989, *NASA Spec. Pub.*, **494**
- Gérard, J.-C., Grodent, D., Radioti, A., Bonfond, B., & Clarke, J. T. 2013, *Icarus*, **226**, 1559
- Gérard, J.-C., Bonfond, B., Grodent, D., et al. 2014, *J. Geophys. Res. (Space Phys.)*, **119**, 9072
- Giorgini, J. D., Yeomans, D. K., Chamberlin, A. B., et al. 1996, in AAS/Division for Planetary Sciences Meeting Abstracts, *BAAS*, **28**, 1158
- Gustin, J., Grodent, D., Ray, L. C., et al. 2016, *Icarus*, **268**, 215
- Hess, S., Cecconi, B., & Zarka, P. 2008a, *Geophys. Res. Lett.*, **35**, L13107
- Hess, S., Mottez, F., Zarka, P., & Chust, T. 2008b, *J. Geophys. Res. (Space Phys.)*, **113**, A03209
- Hess, S., Bonfond, B., Grodent, D., & Zarka, P. 2011, in *EPSC-DPS Joint Meeting 2011*, 791
- Hess, S. L. G., Echer, E., & Zarka, P. 2012, *Planet. Space Sci.*, **70**, 114
- Hess, S. L. G., Echer, E., Zarka, P., Lamy, L., & Delamere, P. A. 2014, *Planet. Space Sci.*, **99**, 136
- Higgins, C. A., Carr, T. D., & Reyes, F. 1996, *Geophys. Res. Lett.*, **23**, 2653
- Higgins, C. A., Carr, T. D., Reyes, F., Greenman, W. B., & Lebo, G. R. 1997, *J. Geophys. Res.*, **102**, 22033
- Higgins, C. A., Thieman, J. R., Fung, S. F., Green, J. L., & Candey, R. M. 1999, *Geophys. Res. Lett.*, **26**, 389
- Imai, K., Wang, L., & Carr, T. D. 1992, *Geophys. Res. Lett.*, **19**, 953
- Imai, M., Imai, K., Higgins, C. A., & Thieman, J. R. 2008, *Geophys. Res. Lett.*, **35**, L17103
- Imai, K., Garcia, L., Reyes, F., Imai, M., & Thieman, J. R. 2011a, *Planetary, Solar and Heliospheric Radio Emissions (PRE VII)*, 179
- Imai, M., Imai, K., Higgins, C. A., & Thieman, J. R. 2011b, *J. Geophys. Res. (Space Phys.)*, **116**, A12233
- Kivelson, M. G., & Southwood, D. J. 2005, *J. Geophys. Res. (Space Phys.)*, **110**, A12209
- Leblanc, Y. 1981, *J. Geophys. Res.*, **86**, 8546
- Leblanc, Y., de La Noe, J., Genova, F., Gerbault, A., & Lecacheux, A. 1981, *A&AS*, **46**, 135
- Leblanc, Y., Gerbault, A., Rubio, M., & Genova, F. 1983, *A&AS*, **54**, 135
- Leblanc, Y., Gerbault, A., & Lecacheux, A. 1989, *A&AS*, **77**, 425
- Leblanc, Y., Gerbault, A., Lecacheux, A., & Boudjada, M. Y. 1990, *A&AS*, **86**, 191
- Leblanc, Y., Gerbault, A., Denis, L., & Lecacheux, A. 1993, *A&AS*, **98**, 529
- Lecacheux, A., Konovalenko, A. A., & Rucker, H. O. 2004, *Planet. Space Sci.*, **52**, 1357
- Nichols, J. D., Badman, S. V., Bunce, E. J., et al. 2009, *Geophys. Res. Lett.*, **36**, L24102
- Prangé, R., Rego, D., Pallier, L., et al. 1998, *J. Geophys. Res.*, **103**, 20195
- Queindec, J., & Zarka, P. 1998, *J. Geophys. Res.*, **103**, 26649
- Queindec, J., & Zarka, P. 2001, *Planet. Space Sci.*, **49**, 365
- Ray, L. C., & Hess, S. 2008, *J. Geophys. Res.: Space Phys.*, **113**, a1218
- Ryabov, V. B., Zarka, P., Hess, S., et al. 2014, *A&A*, **568**, A53
- Saur, J., Neubauer, F. M., Connerney, J. E. P., Zarka, P., & Kivelson, M. G. 2004, Plasma interaction of Io with its plasma torus, eds. F. Bagenal, T. E. Dowling, & W. B. McKinnon, 537
- Terasawa, T., Maezawa, K., & Machida, S. 1978, *Nature*, **273**, 131
- Thieman, J. R. 1979, *NASA STI/Recon Technical Report N*, 79
- Wright, A. N., & Smith, P. R. 1990, *J. Geophys. Res.*, **95**, 3745
- Wu, C. S. 1985, *Space Sci. Rev.*, **41**, 215
- Wu, C. S., & Lee, L. C. 1979, *ApJ*, **230**, 621
- Zarka, P. 1998, *J. Geophys. Res.*, **103**, 20159
- Zarka, P. 2004, *Planet. Space Sci.*, **52**, 1455
- Zarka, P., & Genova, F. 1983, *Nature*, **306**, 767
- Zarka, P., Farges, T., Ryabov, B. P., Abada-Simon, M., & Denis, L. 1996, *Geophys. Res. Lett.*, **23**, 125
- Zarka, P., Queindec, J., & Crary, F. J. 2001, *Planet. Space Sci.*, **49**, 1137
- Zarka, P., Langmayr, D., Gerbault, A., et al. 2002, *Magnetospheres of the Outer Planets Conference, 2002, JHU/APL, Columbia, Md., USA*
- Zarka, P., Cecconi, B., & Kurth, W. S. 2004, *J. Geophys. Res. (Space Phys.)*, **109**, A09S15
- Zarka, P., Tagger, M., & Cecconi, B. 2011, in *Radioastronomie Basses Fréquences, Ecole thématique du CNRS, Goutelas (Loire)*, Proceedings of the conference held 4–8 juin 2007, eds. P. Zarka, M. Tagger, & B. Cecconi (Paris: Observatoire de Paris et Société Française d’Astronomie et d’Astrophysique (SF2A)), 1

Appendix A: Details on the construction of the catalog

We analyzed $\sim 54\,578$ h of observations by the NDA, recorded during 8163 observation sessions from September 18, 1990 to December 31, 2015¹. For the analysis we used a software developed at the Nançay Radio Observatory, illustrated in Fig. A.1. The dynamic spectra in LH and RH polarizations are recorded in an interleaved manner (one spectrum of each polarization alternately every 0.5 s), but they are then considered as simultaneous at a timescale >1 s. The software displays both dynamic spectra simultaneously with a time integration and a contrast that can be adjusted manually. On-the-fly background subtraction (for each frequency) can be applied. Following visual identification of an emission event on the dynamic spectrum where it is more intense (LH or RH), a polygonal contour is drawn around it (using the mouse), and the emission type is selected according to the criteria of Table 1. Following that procedure, 11 463 emission patches were identified, and thus the same number of polygonal contours were produced. For each of them, the software calculates the minimum and maximum frequencies, start and end times, average intensity ($\langle I \rangle$ in dB above the background) of the emission inside the contour, the average intensity in the symmetrical contour in the dynamic spectrum of opposite polarization, and the circular polarization ratio (Stokes V , computed as $(\langle I_{LH} \rangle - \langle I_{RH} \rangle) / (\langle I_{LH} \rangle + \langle I_{RH} \rangle)$). Average intensities and polarization are computed over the pixels inside the emission contour, which have an intensity that is higher than the background. This background corresponds to the Galactic radio spectrum and it is computed at each frequency from the whole daily observation file. True intensity can be reconstructed from the value in dB and the background flux density $S = 2kT/A$ with $T(K) \sim 60\lambda^{2.55}$ and $A(m^2) = \min(24\lambda^2, 3500)$. All these parameters that characterize the emission globally are stored in the database.

During the construction of the database, we noted that for a few observations the polarization was not recorded reliably. In these rare cases we based emission recognition only on the other characteristics defining each emission type and on the occurrence in the $CML - \Phi_{Io}$ plane. As a result we estimate that the fraction of emissions catalogued with an erroneous polarization in the final database is no more than 1%.

At the next step, each contour is interpolated with a time resolution of 1 min, and consecutive events of the same type separated by a gap ≤ 10 min are merged as a single event with global characteristics recomputed accordingly. We ended up with 6203 such emission events. The minimum and maximum frequencies of the event are determined at each round minute (which is the shortest time constant of the database), with frequency accuracy estimated to be better than ± 300 kHz (four channels, resulting from the uncertainty in the visual determination of the emission limits and the subsequent interpolation of the contour). This step is illustrated in Fig. A.2. All these parameters, together with the observation parameters, are stored in the database. When no emission is observed during an observation, only the parameters of the observation session are stored.

Finally, the complete ephemerides (CML, phase and longitude of Io and of the other Galilean satellites plus Amalthea, Jovicentric latitude of the Earth – usually noted D_E – and of the Sun) are computed for each observation session and emission event at a timescale of 1 min and stored in the database, to be easily available when exploiting the catalog. The ephemerides were calculated using JPL-Horizons (Giorgini et al. 1996).

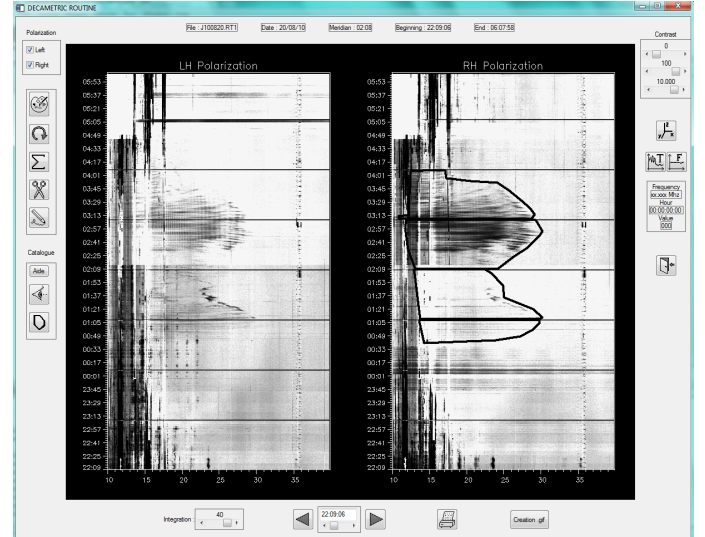


Fig. A.1. Screen capture of the catalog construction software. The LH and RH dynamic spectra for the whole observation of 20/08/2010 are shown. The frequency scale is horizontal (10 to 40 MHz) and the timescale is vertical, increasing upward. This observation lasted for 8 h with a calibration sequence visible every hour. An emission is visible with dominant RH polarization, surrounded by a polygonal contour drawn by hand (with the mouse). The contour was drawn in 4 parts to exclude the calibration sequences of the computed average intensities. The various buttons and tools around the dynamic spectra serve for the interactive display, contour drawing, emission type selection, and recording.

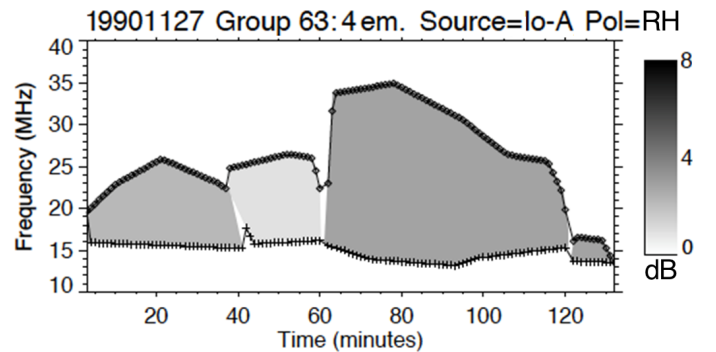


Fig. A.2. Control plot from the second step of catalog construction: merging into a single event group of the events of the same type (here 4 Io-A regions, with RH polarization, on 27/11/1990), separated by a gap ≤ 10 min. The average intensity of each emission is shown in gray levels; F_{\max} (diamonds) and F_{\min} (plus) are determined at 1-min resolution along the interpolated contours.

The phase of Io (Φ_{Io}) is calculated as the departure of its superior geocentric conjunction measured in projection on the equatorial plane of Jupiter. This phase was computed in four steps: (1) the $CML(t)$, i.e., the central meridian longitude in the System III coordinate, is obtained from the ephemeris server, at consecutive observation times at Earth t_E , taking into account the light travel time between Jupiter and Earth dt_E ; (2) Io's longitude $\Lambda_{Io}(t)$ is obtained similarly, setting Io as the observer, at consecutive times at Io t_{Io} with a light travel time dt_{Io} ; these angles are derotated as a monotonously increasing series over the 26 yr studied; (3) $\Lambda_{Io}(t)$ is reinterpolated from a time axis t_E to a time axis $t_E - (dt_E - dt_{Io})$, to correct for the different travel times; and (4) the phase, for example, of Io, is derived as $\Phi_{Io}(t) = CML(t) - \Lambda_{Io}(t) + 180^\circ$, and angles are finally set

¹ These data can be accessed at <https://www.obs-nancay.fr/>

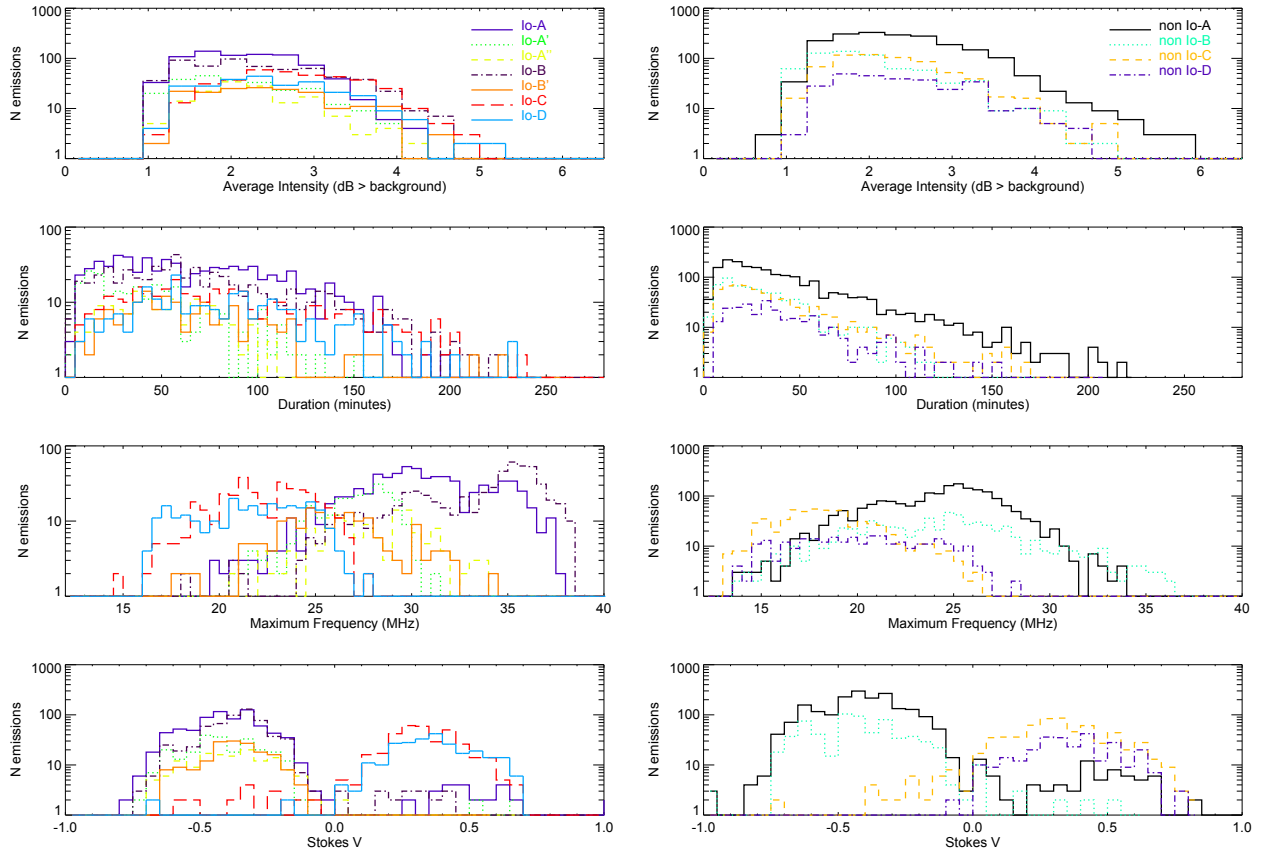


Fig. B.1. Histograms of intensity, duration, maximum frequency, and circular polarization of Io (*left*) and non-Io (*right*) emission types.

back into the range $[0^\circ, 360^\circ]$. Likewise, this was performed for Europa, Ganymede, Callisto, and Amalthea.

Appendix B: Plots per emission type

We provide here complementary plots to Sects. 4.2 and 4.3. Figure B.1 is similar to the histograms of Figs. 8–10 but sorted by emission type, whereas Fig. B.2 complements Fig. 13, also sorted by emission type.

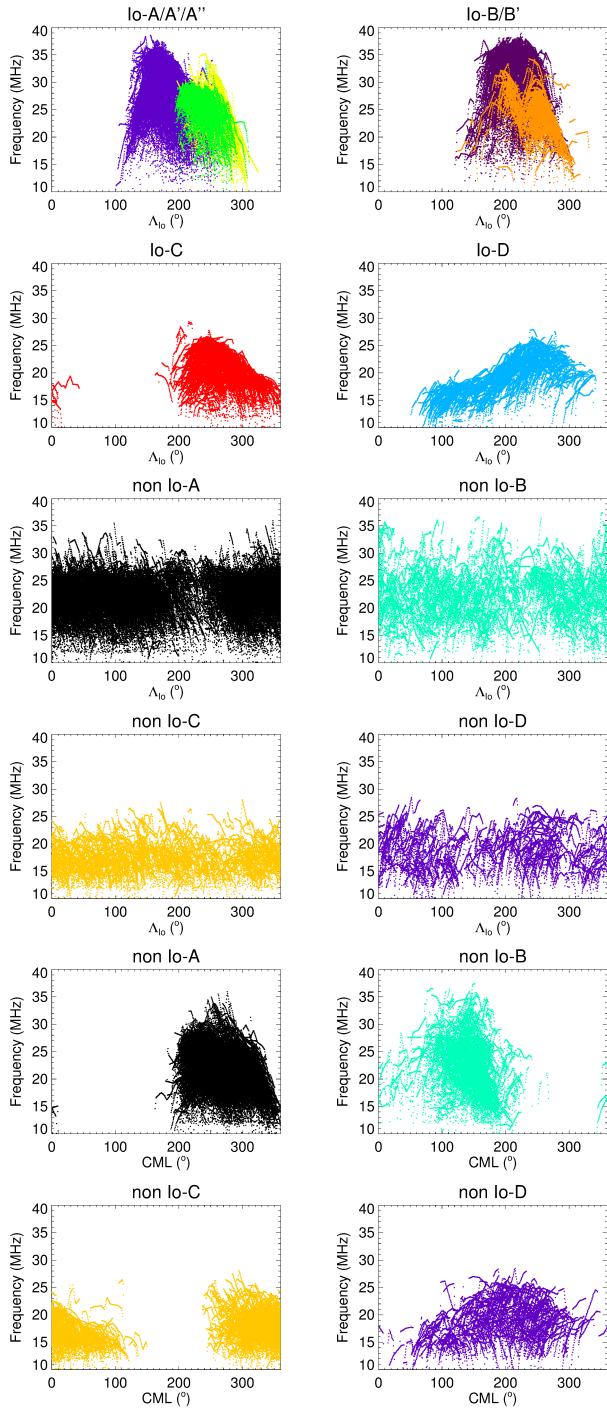


Fig. B.2. Maximum frequency envelopes of Io emission types vs. Λ_{Io} and non-Io emission types vs. Λ_{Io} and CML at the time resolution of 1 minute.